

Multi-proxy records of wildfires and climate-vegetation-wildfire interactions during the Middle Jurassic of the Santanghu Basin, northwest China

Jiamin Zhou^a, Longyi Shao^{a,*}, Timothy P. Jones^b, Yangyang Huang^a, Mengran Chen^a, Yuedong Ma^a, Jing Lu^a

^a State Key Laboratory for Fine Exploration and Intelligent Development of Coal Resources and College of Geoscience and Surveying Engineering, China University of Mining and Technology (Beijing), Beijing 100083, China

^b School of Earth and Environmental Sciences, Cardiff University, Cardiff CF10 3YE, Wales, UK

ARTICLE INFO

Editor: H Falcon-Lang

Keywords:

Middle Jurassic
Inertinite
Natural char
PAHs
Palaeowildfires
Paleoenvironment

ABSTRACT

Palaeowildfires have played an important role in terrestrial ecosystems since the evolution of land plants, and are a significant disturbance factor in many of the Earth's ecosystems. The Middle Jurassic was a period of rapid climatic fluctuations, and there is abundant evidence that wildfires were frequent at that time. The Santanghu Basin has Middle Jurassic inertinite-rich coals that are a source of high-quality information about palaeowildfires and palaeoenvironments; these provide an opportunity to study deep-time palaeowildfire evolution and their ecological effects. To better understand palaeowildfire events, a multi-proxy study was undertaken that analyzed coal macerals, inertinite reflectance, and polycyclic aromatic hydrocarbons (PAHs) in coal and mudstone samples from the Aalenian Santanghu Basin. In addition, normal alkanes (*n*-alkanes) were used as biomarkers of alterations in coal-forming vegetation, and natural char was used as complementary coal petrological evidence for palaeowildfires. The presence of high levels of inertinite, high natural char content, and high abundances of potentially combustion-derived PAHs demonstrate that multiple, widespread wildfires occurred during the Aalenian in the Santanghu Basin. Inertinite reflectance values ranging from 1.34 % to 2.67 %Ro indicate that palaeowildfires were dominated by lower temperature ground fires, with a small proportion of higher temperature crown fires. It is believed that the total amount of PAHs can be used as good evidence of palaeowildfires, but the ratios of high to low ring PAHs in the molecules are not necessarily indicative of combustion temperatures of palaeowildfires due to the extreme instability of low-ring PAHs. It is proposed that the abundant inertinites in Jurassic coals were accumulated as the result of a multi-factorial coupling; palaeoclimate was the main driver, paleo vegetation and gelified organic matter provided the fuel, and palaeowildfires were indirectly the mechanism of preservation. Furthermore, a potential mechanism has been proposed for wildfire activity to influence the growth of aquatic plants.

1. Introduction

In recent years, rising global temperatures continue to increase, and the rapid planetary warming has been accompanied by a series of extreme climate events, including wildfires (Scott, 2010; Zheng et al., 2023; WMO, 2024). Wildfires have received serious attention for their impact on the environment, ecosystems and humans, and there is an urgent need to investigate and better understand the evolution of wildfire regimes longer timescales (Marlon, 2020; McLauchlan et al.,

2020; Jones et al., 2024). The Jurassic, especially the Middle Jurassic, was a period of rapid climatic change (Judd et al., 2024), and as such is an ideal period for the study of Earth's terrestrial ecosystems. The Jurassic coals in northern China are unusually rich in inertinites (Yang, 1996; Xu et al., 2020; Xie et al., 2022; Zhou et al., 2024), which provide an opportunity to study the deep-time evolution of wildfires and their ecological effects (Zhang et al., 2020; Zhao et al., 2023).

Changes in wildfire activities in deep-time can be identified in the geological records through variations in the amounts of preserved

* Corresponding author.

E-mail address: ShaoL@cumtb.edu.cn (L. Shao).

products of combustion, such as much of the inertinite group that are widely accepted as fossil charcoal, pyrogenic polycyclic aromatic hydrocarbons (PAHs) and natural char (Kwiecinska and Petersen, 2004; Scott and Glasspool, 2007; Marynowski et al., 2011; Baker, 2021; Han et al., 2024). Observations on modern charring experiments strongly support the view that fusinite and most semifusinite, are the products of the incomplete combustion of plant materials (Jones, 1997; Scott and Glasspool, 2007). Many inertodetrinite particles are relics from palaeowildfires in or around peatlands, and macrinite in low-rank coals may have formed in smoldering peat fires (ICCP, 2001). Dai et al. (2015) found fecal pellets in degraded plant tissues, which were burnt in wildfires to form macrinite assemblages. Other macerals of the inertinite group that may not be derived from fires (Stach et al., 1982; Taylor et al., 1998; Dai et al., 2020), but they are generally present at amounts below 10 % (Diessel, 2010; Zhou et al., 2024).

One of the main sources of PAHs in the sedimentary record is the incomplete combustion of biomass (Yunker et al., 2012; Zakir Hossain et al., 2013). Many studies have used PAHs as biomarker proxies of palaeowildfires (Karp et al., 2020; Fox et al., 2022a; Zhao et al., 2023; Han et al., 2024). It is important to note that the physical properties of PAHs vary considerably in different components, ranging from slightly soluble in water (Naphthalene) to extremely insoluble (BghiP), and from volatile (Naphthalene) to semi-volatile (Perylene) (Lima et al., 2005). In comparison, PAHs with three or fewer rings are physically and chemically unstable and are more difficult to preserve during sedimentation. Consequently some discriminant ratios such as 5/3-ringed PAHs and 6/3-ringed PAHs need to be used with caution (Karp et al., 2020).

According to Kwiecinska and Petersen (2004), natural char can be defined as having “a higher reflectance than the associated huminite/vitrinite, and commonly the reflectance is also higher than the associated inertinite” and is characterized by a “random distribution of pores and a varying porosity”. Fossilized natural char is also gradually being adopted as additional evidence of palaeowildfire (Xu et al., 2020; Nádudvari et al., 2023; Han et al., 2024).

The *n*-alkane biomarkers provide considerable insights into palaeoenvironmental reconstruction (Ficken et al., 2000; Liu et al., 2022b). Different chain lengths of *n*-alkanes can indicate different types of palaeovegetation, with the long-chain *n*-alkanes (C₂₇ - C₃₃) generally originating from terrestrial higher plants and water-supporting plants, the medium-chain long *n*-alkanes (C₂₁ - C₂₅) being produced mainly by floating and submerged plants, and the short-chain *n*-alkanes (C₁₅ - C₁₉) being derived from photosynthesising bacteria and algae (Meyers and Ishiwatari, 1993; Street-Perrott et al., 2004; Castañeda and Schouten, 2011). As a result, *n*-alkanes can be used as evidence for the evolution of plant populations for the establishment of climate-fuel-fire relationships (Baker, 2021).

The comprehensive body of research in palaeowildfires in the Jurassic has convincingly established that wildfires were a globally widespread natural phenomenon at that time (Marynowski and Simoneit, 2009; Marynowski et al., 2011; Baker et al., 2017; Hollaar et al., 2021; Wang et al., 2021; Hou et al., 2022; Xie et al., 2022; Zhou et al., 2024). The intensity, frequency and type of wildfire activity is influenced by climate, vegetation, and atmospheric compositions (Scott, 2000). The Middle Jurassic was a representative greenhouse period in the Earth's history with frequent climate fluctuations (Judd et al., 2024), with high global mean surface temperature (Scotese et al., 2021; Judd et al., 2024), high atmospheric oxygen content (Mills et al., 2023; Zhou et al., 2024), high atmospheric carbon dioxide levels (Judd et al., 2024).

The Santanghu Basin in northwestern China has thick Jurassic terrestrial strata and multi-layered thick inertinite-rich coal seams, and this presents an excellent opportunity to study the evolution of Jurassic terrestrial ecosystems. Numerous previous studies have focused on the sedimentology, palaeoclimate stratigraphy and coal accumulation in the Lower-Middle Jurassic coal-bearing series of the Santanghu Basin (Feng et al., 2019; Gou et al., 2021; Zhang et al., 2023; Yang et al., 2024), however, there is a distinct lack of research on palaeoclimate and

palaeoenvironmental evolution and the possible relationships between wildfires, vegetation, and climate (Xu et al., 2020; Zhou et al., 2024). Jurassic coals in the Santanghu Basin containing abundant natural char can also provide new evidence for palaeowildfire research, and biomarkers of plants are useful additions to the palaeovegetation reconstruction of the Middle Jurassic.

An analysis of maceral compositions, inertinite characteristics, PAHs, and *n*-alkanes of the coal and mudstones in the Xishanyao Formation of the early Middle Jurassic in the Santanghu Basin was undertaken. Based on these diverse data, we identify palaeowildfire multi-proxy records and palaeowildfire types and propose feedback relationships between palaeoclimate, palaeovegetation and palaeowildfire. These patterns of climate-fuel-fire relationships may provide a deep-time perspective for future understanding of changing levels of wildfire occurrences on a globally warming planet.

2. Geological setting

The Santanghu Basin is located in the northeastern part of the Xinjiang Uygur Autonomous Region in Northwest China, and is a narrow strip, extending from NW to SE (Fig. 1) (Zhao et al., 2003). The basin is approximately 500 km long and the central depression is about 40–70 km wide, with a total area of about 2.3×10^4 km² (Liu et al., 2010). Tectonically, the basin is a superimposed modified basin on the Early Paleozoic basement, distributed between the Altai Mountain System and the East Tianshan Mountain System (Allégre et al., 1984; Hendrix et al., 1992; Li, 1995).

Since the Late Permian, the basin has undergone three stages of development: the foreland basin stage, the extensional depression stage and the foreland basin resurrection (Zhao et al., 2003; Liu et al., 2010). The current tectonic structure from southwest to northeast is the Southwest thrust nappe zone, the Central depression belt and the Northeast thrust uplift zone, respectively. The central depression belt can be subdivided into 11 sub-tectonic units from northwest to southeast, including Kumusu Sag, Baruntala Uplift, Hanshuiquan Sag, Shitoumei Uplift, Tiaohu Sag, Chahaquan Uplift, Malang Sag, Fangfangliang Uplift, Naomaohu Sag, Weibei Uplift, and Suluke Sag (Liu et al., 2017).

The Jurassic strata are widely developed in the Santanghu Basin, and the Middle Jurassic consists of the Xishanyao Formation (J_{2x}) and the Toutunhe Formation (J_{2t}). The Xishanyao Formation is the main coal-bearing strata, and the total thickness of the coal seams ranges from 0.34 to 51.5 m, with an average thickness of 18.7 m (Li and Zhao, 2015; Feng et al., 2018).

The results of sporo-pollen analysis in the Santanghu Basin show that the Xishanyao Formation has developed the *Osmundacidites-Quadraculina-Perinopollenites* assemblage, which corresponds to the Early Middle Jurassic, i.e., from the Aalenian to Bajocian Stages, and it can be compared with sporo-pollen assemblages of contemporaneous stratigraphy from around the world (Huang, 2002, 2003; Yang et al., 2024).

3. Materials and methods

The coal samples were collected from the Tangqican1 (Tqc-1) well in the Malang sag (Fig. 1). A total of 40 samples were collected, including 29 coal samples and 11 mudstone samples. The simple continuous inequidistant sampling methods were used (Tables 1 and 2). All samples were stored immediately in airtight plastic bags to protect them from contamination and oxidation. In addition, this paper produced charcoal from modern Cyathea by charcoalfication experiments.

In the laboratory, the coal samples were air-dried, crushed to a maximum grain size of 1 mm, and prepared as polished epoxy-bound pellets for petrographic analyses. The different maceral contents and reflectance of coal samples were determined under white reflected and fluorescent light, with a 40× oil-immersion objective using a Leica DM2700 reflected light microscope equipped with TIDAS J&M MSP300

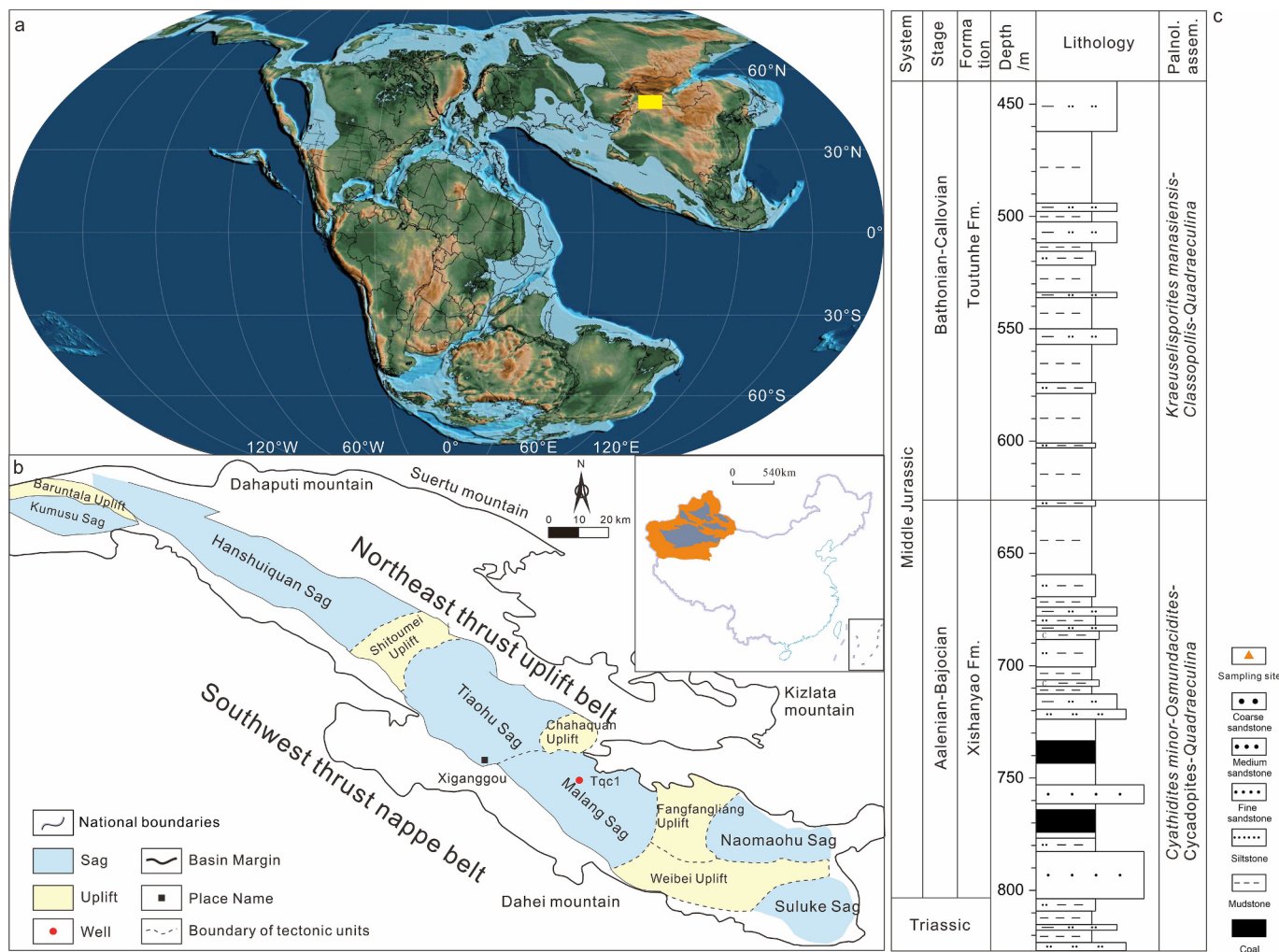


Fig. 1. Palaeoplate location, division of tectonic units and Middle Jurassic stratigraphy of Santanghu Basin. **a.** Global plate distribution of the Middle Jurassic showing position of Santanghu Basin (modified after [Scotese and Wright \(2018\)](#)). **b.** Outline map of China showing position of Santanghu Basin with tectonic features (modified after [Liu et al. \(2017\)](#)). **c.** Stratigraphic succession for the Tqc-1 well during the Middle Jurassic interval with palynological assemblages, palynological assemblages from [Huang \(2002\)](#).

microphotometer at the State Key Laboratory for Fine Exploration and Intelligent Development of Coal Resources based in China University of Mining and Technology (Beijing).

Maceral classification and terminology in this study follow ICCP protocols ([ICCP, 2001](#); [Sýkorová et al., 2005](#); [Pickel et al., 2017](#)), and for maceral analyses, approximately 500 points in each polished block were counted ([ISO, 2009a](#)). For inertinite and vitrinite reflectance measurements, Cubic Zirconia (CZ) (2.96 %), Yttrium Aluminium Garnet (YAG) (0.901 %), Sapphire (0.595 %) and optically black (zero) were employed, with approximately 60 points counted separately for vitrinite group and inertinite group ([ISO, 2009b](#)). This study focuses on inertinite reflectance measurements of fusinite, semifusinite and inertodetrinitite. For observation of homogenized cell walls, small fusain fragments were mounted on a standard stub, coated with gold, and then observed under a Thermo Apreo 2C Scanning Electron Microscope (SEM) at the Key Laboratory of Transparent Mine Geology and Digital Twin Technology, National Mine Safety Administration.

The charring temperatures were estimated based on the average inertinite reflectance value and calculated by established inertinite reflectance-temperature relationship $T = 184.10 + 117.76 \times \%R_o$ ($r^2 = 0.91$), where T is the burning temperature, with unit of $^{\circ}\text{C}$, and R_{lo} is the measured inertinite reflectance, with unit of % ([Jones, 1997](#)). From the charring temperatures, palaeowildfires can, in simple terms, be

categorized into three types: ground fires, surface fires, and crown fires ([Scott, 1989](#); [Scott, 2010](#)). In this paper, the inertinite reflectances of 1.5 % and 3.5 %, corresponding to burning temperatures of about $360\ ^{\circ}\text{C}$ and $600\ ^{\circ}\text{C}$, respectively, are used as a boundary (ground fires $\leq 1.5\ \% R_o$ [$\sim 360\ ^{\circ}\text{C}$]; surface fires 1.5–3.5 % R_o [$\sim 360\ ^{\circ}\text{C}$ to $\sim 600\ ^{\circ}\text{C}$]; crown fires $\geq 3.5\ \% R_o$ [$\sim 600\ ^{\circ}\text{C}$]) to discriminate between wildfire types ([Scott, 2010](#)).

Prior to GC-MS analyses, cleaned, powdered samples were treated with dichloromethane using the Soxhlet extraction techniques for 48 h to separate the soluble organic matter. The identification and quantification of aromatic hydrocarbon fractions in the extracts were analyzed using a gas chromatograph-mass spectrometer (GC-MS; Shimadzu QC-2030) in the Research Center of Applied Geology of China Geological Survey based in Chengdu. The GC-MS analysis of aromatic hydrocarbon fractions follows the methods of [Fox et al. \(2022a\)](#), and the identification and quantification of *n*-alkanes follows the methods of [Li et al. \(2022a\)](#).

4. Results

4.1. Coal petrology

Three groups of macerals, including vitrinite, liptinite and inertinite,

Table 1

Maceral compositions and inertinite reflectance values of coal samples from the Middle Jurassic Xishanyao Formation in the Santanghu Basin.

Sample no.	Depth	Maceral composition (vol%; on mineral-free basis)														Vitrinite reflectance (%Ro)	Inertinite and natural char reflectance (%Ro)						
		F	SF	Fun	Sec	Mac	Mic	ID	T-I	T	CT	VD	CD	CG	G	T-V	T-L	Natural char	Aver.	Max.	Min.		
1-42/52	716.72	0.6	2.2	0	0	0.8	0	3.9	7.5	1.4	34.2	0.8	39.4	9.4	0	85.3	7.2	0	2.31	4.35	0.98		
2-22/61	721.26	7.2	32.9	0.3	1.4	1.9	0	19.1	62.7	3.3	0.8	1.4	23.8	1.9	0	31.2	0	6.1	1.88	4.07	0.85		
2-25/61	721.84	15.8	24.6	1.3	0.6	3.9	1.7	4.8	52.5	7.2	9	0.7	21.8	2.8	0	41.5	0.6	5.4	2.51	5.7	0.51		
2-35/61	723.09	19	39.5	0	1	1.4	0	11.5	72.4	9.3	1	1.4	4.2	2.8	0	18.8	1.2	7.6	1.53	3.99	0.43		
2-36/61	724	18.3	9.9	0	0	2.9	2	2.3	35.4	40.9	2.3	0	13.8	4.3	0	61.2	0.2	3.2	2.58	5.7	0.6		
2-44/61	724.81	22.2	15.7	0	0.9	3	0.2	6	48.1	10.3	19.4	0	19.2	0.9	0	49.8	0	2.1	0.35	2.67	5.74	0.68	
3-13/65	729.13	11.4	28.7	0.4	0.4	2.2	0.4	19.1	62.5	6.1	3.1	0.2	12.8	2.9	0	25.1	0	12.4	1.99	5.74	0.56		
3-62/65	734.97	8.7	22.8	0	0	2.1	0	14.4	47.8	3	7.7	0.5	29.8	5.9	0	46.9	0.2	5.1	0.35	2.03	4.81	0.7	
4-5/53	736.13	17.6	30.3	0.2	0.4	2.6	0	15.7	66.9	9.9	1.7	0.2	4.5	8.2	0	24.5	0	8.6	1.68	4.36	0.6		
4-11/53	736.83	10.2	12.4	0	0	0.5	0	7.7	30.8	6.5	46	0	14.2	1.5	0	68.2	0	1	0.33	2.13	5.99	0.61	
4-15/53	737.43	13.8	20.4	0.2	0.7	1.6	0.2	12.4	49.3	6.9	6.4	0	26.7	6.7	0.2	46.9	0.2	3.6	1.68	6.25	0.54		
4	4-19/53	738.43	14.9	22.7	0	0.5	2.3	0.5	10.8	51.6	11.5	5	0	18	9	0	43.5	0	4.9	1.67	5.7	0.55	
	4-27/53	739.03	21.1	26.3	0	0.3	1.4	0.6	12.5	62	7.8	0.6	2.2	15.8	8.6	0.3	35.2	0	2.8	1.53	3.88	0.59	
	4-31/53	740.03	25.9	18.6	0.3	0	2.2	0	20.3	67.3	2.4	0.5	6.2	11.1	8.1	0.8	29.2	0.5	3	1.39	5.9	0.42	
	4-35/53	740.96	8.3	3.3	0.2	0	0.4	0.9	7.1	20.3	10	17.9	0.4	44.4	4.7	0	77.5	2	0.2	0.32	1.34	3.76	0.38
	4-40/53	741.73	29.5	25.9	0	0.2	1	0	16.9	73.6	4.6	0.8	0.6	15.5	3.8	0	25.3	0	1.1	1.69	4.79	0.48	
	4-46/53	742.32	11.9	19.5	0.3	0.3	1	0.3	19.3	52.7	6.5	2.3	5.4	19.1	9.2	0.3	42.9	0	4.4	1.74	6.08	0.51	
	4-53/53	743.62	14.1	19.6	0	0.2	1.8	0.3	12.1	48.1	6.6	3.6	3.4	19.6	15	0.2	48.4	0.2	3.3	2	5.08	0.56	
	5-3/38	744.57	11.9	12.7	0	0.4	3.1	0	10.9	39	5.7	8.4	0.4	36.3	6.6	0.2	57.7	2.1	1.2	1.92	5.41	0.63	
	5-9/38	745.66	17.3	21.2	0	0	2.1	0	2.3	42.9	4.7	9.5	2.3	30.3	6.1	0	52.9	0.2	4	0.35	1.56	4.41	0.69
	5-14/38	746.14	12.9	19	0.3	0.6	3.3	0.2	18.5	54.7	7.9	1.7	1.7	18.5	9	0	38.9	0	6.4	1.85	6.3	0.54	
	5-22/38	747.35	9.4	16	0.4	0.6	2.2	0	13.9	42.7	7.9	7.8	1.5	30.8	6.6	0	54.6	0.7	2	1.91	6.55	0.7	
	5-29/38	748.03	15.7	14.8	0.3	0.6	1.1	0	11.9	44.4	8.5	3.6	1.4	32.7	3.9	0.3	50.4	1.4	3.8	2.1	6	0.53	
	5-34/38	749.03	12.2	8.8	0	0	0	0	13.8	34.8	9.2	8.4	13.8	29.6	1.3	0	62.3	2.5	0.4	2.12	4.38	0.63	
	6-42/70	755.65	22.1	15.6	0.2	0.7	1.3	0	8.8	48.7	7.7	5.1	0.6	31.3	3.7	0	48.3	0.4	2.6	2	6.43	0.84	
	6-44/70	756.13	18.5	11.7	0	0	0.2	0	3.7	34.1	6.4	26.4	0	31.1	1.3	0	65.2	0	0.7	0.33	2.22	6.15	0.55
	6-64/70	757.21	8.1	6.4	0	0	0.3	0	6.7	21.5	0.8	40.1	0	33.7	1	0	75.7	0.3	2.5	2.2	6.75	0.75	

F, fusinite; SF, semifusinite; Mic, micrinite; Mac, macrinite; Sec, secretinite; Fun, funginite; ID, inertodetrinite; T-I, total inertinites; T, telinite; CT, collotelinite; VD, vitrodetrinite; CD, collodetrinite; CG, corpogelinite; G, gelinite; T-V, total vitrinites; T-L, total liptinites. Min., minimum; Max., maximum; Ave., average.

Table 2

Concentrations and ratios of PAHs in coal and mudstone samples of the Middle Jurassic Xishanyao Formation of the Santanghu Basin.

Sample no.	1–5/52	1–28/52	1–37/52	1–42/52	1–49/52	2–16/61	2–22/61	2–25/61	2–35/61	2–36/61	2–44/61	3–3/65	3–13/65
Sample depth	710.1	713.9	715.6	716.72	717.2	720.26	721.26	721.84	723.09	724	724.81	727.49	729.13
Lithology	Mudstone	Mudstone	Mudstone	Coal	Mudstone	Mudstone	Coal	Coal	Coal	Coal	Coal	Coal	Coal
Naphthalene (2)	0.002	0.002	0	0.095	0.001	0.002	0.051	0.155	0.297	0.056	0.025	0.034	0.028
Acenaphthylene (3)	0	0	0.002	0.02	0	0	0.017	0.063	0.048	0.032	0.014	0.022	0.006
Acenaphthene (3)	0	0	0.002	0.008	0	0	0.013	0.013	0.03	0.02	0.009	0.02	0.005
Fluorene (3)	0.001	0.001	0.003	0.032	0	0.001	0.047	0.085	0.122	0.053	0.02	0.105	0.027
Phenanthrene (3)	0.14	0.065	0.422	0.372	0.087	0.129	1.192	2.256	3.38	2	0.744	3.212	0.776
Anthracene (3)	0.005	0.004	0.387	0.017	0.003	0.008	0.293	0.572	0.887	0.261	0.076	0.437	0.109
Fluoranthene (4)	0.034	0.019	0.355	0.489	0.045	0.045	1.502	3.319	5.027	2.382	0.853	2.49	0.664
Pyrene (4)	0.019	0.013	0.22	0.309	0.035	0.032	1.296	2.604	3.42	1.292	0.522	1.281	0.435
Benz[a]anthracene (4)	0.003	0.003	0.061	0.139	0.008	0.009	1.043	1.465	3.001	0.422	0.108	1.312	0.27
Chrysene (4)	0.002	0.002	0.028	0.08	0.006	0.007	0.541	0.734	1.088	0.219	0.049	0.503	0.103
Benz[j]fluoranthene (5)	0	0	0.033	0	0	0	0.661	0.506	0.834	0.001	0.007	0.398	0.065
Benz[b]fluoranthene (5)	0	0	0.06	0	0.003	0	1.194	0.915	0.384	0.001	0.013	0.171	0.118
Benz[k]fluoranthene (5)	0	0	0.014	0.016	0	0	0.226	0.148	0.224	0.042	0.009	0.105	0.001
Benz[a]pyrene (5)	0	0	0.007	0.022	0.003	0	0.203	0.221	0.586	0.063	0.01	0.196	0.017
Indeno[1,2,3-c,d]pyrene (6)	0	0	0.005	0.016	0	0.001	0.241	0.101	0.007	0.023	0	0.084	0.02
Dibenz[a,h]anthracene (5)	0	0	0	0.002	0	0	0.036	0.011	0.08	0.004	0	0.022	0.002
Benz[g,h,i]perylene (6)	0	0	0.004	0.006	0.002	0	0.099	0.042	0.098	0.011	0.003	0.035	0.007
Total	0.206	0.108	1.603	1.624	0.195	0.238	8.655	13.212	19.514	6.881	2.463	10.427	2.654
3-ring	0.146	0.07	0.816	0.449	0.09	0.138	1.562	2.989	4.467	2.366	0.863	3.796	0.923
4-ring	0.058	0.037	0.664	1.017	0.094	0.093	4.382	8.122	12.536	4.315	1.532	5.586	1.472
5-ring	0	0	0.114	0.046	0.006	0	2.428	1.834	2.348	0.123	0.039	0.958	0.209
6-ring	0	0	0.009	0.022	0.002	0.001	0.34	0.143	0.105	0.034	0.003	0.119	0.027
3-ringed/Total	70.9	64.8	50.9	27.6	46.2	58	18	22.6	22.9	34.4	35	36.4	34.8
4-ringed/Total	28.2	34.3	41.4	62.6	48.2	39.1	50.6	61.5	64.2	62.7	62.2	53.6	55.5
5-ringed/Total	0	0	7.1	2.8	3.1	0	28.1	13.9	12	1.8	1.6	9.2	7.9
6-ringed/Total	0	0	0.6	1.4	1	0.4	3.9	1.1	0.5	0.5	0.1	1.1	1
Fla/(Fla + Pyr)	0.64	0.59	0.62	0.61	0.56	0.58	0.54	0.56	0.6	0.65	0.62	0.66	0.6
BaA/(BaA + Chr)	0.6	0.6	0.69	0.63	0.57	0.56	0.66	0.67	0.73	0.66	0.69	0.72	0.72
InPy/(InPy + BghiP)	0	0	0.56	0.73	0	1	0.71	0.71	0.07	0.68	0	0.71	0.74
5-ringed/3-ringed	0	0	0.14	0.1	0.07	0	1.55	0.61	0.53	0.05	0.05	0.25	0.23
6-ringed/3-ringed	0	0	0.01	0.05	0.02	0.01	0.22	0.05	0.02	0.01	0	0.03	0.03

Sample no.	3–48/65	3–56/65	3–59/65	3–62/65	4–5/53	4–11/53	4–15/53	4–19/53	4–27/53	4–31/53	4–35/53	4–40/53	4–46/53
Sample depth	732.4	734.24	734.69	734.97	736.13	736.83	737.43	738.43	739.03	740.03	740.96	741.73	742.32
Lithology	Mudstone	Mudstone	Coal	Coal	Coal	Coal	Coal	Coal	Coal	Coal	Coal	Coal	Coal
Naphthalene (2)	0.016	0.002	0.005	0.01	0.008	0.037	0.051	0.045	0.029	0.024	0	0.056	0.009
Acenaphthylene (3)	0.003	0.002	0.002	0.014	0.013	0.02	0.016	0.014	0.009	0.007	0.028	0.016	0.002
Acenaphthene (3)	0.002	0.001	0	0.001	0.003	0.003	0.004	0.002	0.003	0.001	0.004	0.002	0.001
Fluorene (3)	0.004	0.002	0.001	0.002	0	0.005	0.005	0.009	0.008	0.004	0.001	0.006	0.003
Phenanthrene (3)	1.784	1.393	0.052	0.065	0.148	0.293	0.109	0.188	0.15	0.21	0.121	0.297	0.096
Anthracene (3)	0.027	0.021	0.006	0.031	0.072	0.076	0.046	0.049	0.036	0.056	0.05	0.072	0.031
Fluoranthene (4)	1.474	0.681	0.172	0.315	1.714	2.43	1.479	1.322	0.361	1.211	1.124	1.182	0.764
Pyrene (4)	0.425	0.219	0.103	0.73	1.434	2.347	1.471	2.027	0.984	1.461	2.934	1.452	1.044
Benz[a]anthracene (4)	0.159	0.079	0.077	0.418	1.893	1.25	1.093	1.276	0.476	0.457	0.949	0.714	0.399
Chrysene (4)	0.081	0.046	0.07	0.68	1.682	1.544	1.249	0.79	1.195	0.772	1.82	1.18	1.121
Benz[j]fluoranthene (5)	0.045	0.003	0	0.504	1.027	0.924	0.724	0.647	1.06	0.638	1.095	0.776	0.904
Benz[b]fluoranthene (5)	0.082	0.005	0	0.911	0.444	1.673	1.309	0.271	1.918	1.154	1.979	1.403	1.635
Benz[k]fluoranthene (5)	0.005	0	0.032	0.279	0.502	0.536	0.368	0.331	0.592	0.006	0.621	0.427	0.553
Benz[a]pyrene (5)	0.001	0	0.02	0.262	0.504	0.309	0.251	0.305	0.46	0.187	0.246	0.225	0.235
Indeno[1,2,3-c,d]pyrene (6)	0.004	0.003	0.012	0.094	0.004	0.123	0.091	0.099	0.173	0.11	0.13	0.106	0.114
Dibenz[a,h]anthracene (5)	0	0	0.002	0.017	0.03	0.022	0.018	0.02	0.035	0.019	0.02	0.02	0.021
Benz[g,h,i]perylene (6)	0.001	0	0.012	0.049	0.085	0.053	0.05	0.063	0.113	0.091	0.044	0.068	0.09
Total	4.116	2.458	0.564	4.379	9.562	11.645	8.335	7.459	7.603	6.408	11.167	8.001	7.02
3-ring	1.82	1.419	0.061	0.113	0.236	0.397	0.18	0.262	0.206	0.278	0.204	0.393	0.133
4-ring	2.139	1.025	0.422	2.143	6.723	7.571	5.292	5.415	3.016	3.901	6.827	4.528	3.328
5-ring	0.133	0.008	0.06	2.024	2.597	3.53	2.724	1.634	4.17	2.061	4.021	2.911	3.411
6-ring	0.005	0.003	0.024	0.143	0.089	0.176	0.141	0.162	0.286	0.201	0.174	0.174	0.204
3-ringed/Total	44.2	57.7	10.8	2.6	2.5	3.4	2.2	3.5	2.7	4.3	1.8	4.9	1.9
4-ringed/Total	52	41.7	74.8	48.9	70.3	65	63.5	72.6	39.7	60.9	61.1	56.6	47.4
5-ringed/Total	3.2	0.3	10.6	46.2	27.2	30.3	32.7	21.9	54.8	32.2	36	36.4	48.6
6-ringed/Total	0.1	0.1	4.3	3.3	0.9	1.5	1.7	2.2	3.8	3.1	1.6	2.2	2.9
Fla/(Fla + Pyr)	0.78	0.76	0.63	0.3	0.54	0.51	0.5	0.39	0.27	0.45	0.28	0.45	0.42
BaA/(BaA + Chr)	0.66	0.63	0.52	0.38	0.53	0.45	0.47	0.62	0.28	0.37	0.34	0.38	0.26
InPy/(InPy + BghiP)	0.8	1	0.5	0.66	0.04	0.7	0.65	0.61	0.6	0.55	0.75	0.61	0.56
5-ringed/3-ringed	0.07	0.01	0.98	17.91	11	8.89	15.13	6.24	20.24	7.41	19.71	7.41	25.65
6-ringed/3-ringed	0	0	0.39	1.27	0.38	0.44	0.78	0.62	1.39	0.72	0.85	0.44	1.53

Sample no.	4–53/53	5–3/38	5–9/38	5–14/38	5–22/38	5–29/38	5–34/38	5–37/38	6–7/70	6–42/70	6–44/70	6–49/70	6–54/70	6–64/70
------------	---------	--------	--------	---------	---------	---------	---------	---------	--------	---------	---------	---------	---------	---------

(continued on next page)

Table 2 (continued)

Sample no.	4–53/53	5–3/38	5–9/38	5–14/38	5–22/38	5–29/38	5–34/38	5–37/38	6–7/70	6–42/70	6–44/70	6–49/70	6–54/70	6–64/70
Sample depth	742.62	744.57	745.66	746.14	747.35	748.03	749.03	749.28	750.53	755.65	755.98	756.9	757.21	757.64
Lithology	Coal	Coal	Coal	Coal	Coal	Coal	Coal	Mudstone	Mudstone	Coal	Coal	Mudstone	Coal	Mudstone
Naphthalene (2)	0.011	0.024	0.015	0.006	0.009	0.008	0.01	0.007	0.003	0.119	0.008	0.004	0.025	0.006
Acenaphthylene (3)	0.023	0.018	0.078	0.026	0.025	0.018	0.018	0.005	0.001	0.054	0.039	0.002	0.048	0.002
Acenaphthene (3)	0.002	0.002	0.003	0.005	0.002	0.002	0.001	0.001	0	0.016	0.008	0	0.009	0
Fluorene (3)	0.005	0.003	0.001	0.007	0.001	0.001	0.011	0.003	0	0.061	0.042	0.001	0.029	0.002
Phenanthrene (3)	0.166	0.187	0.228	0.284	0.179	0.347	0.23	0.196	0.103	5.504	5.921	0.383	6.24	0.441
Anthracene (3)	0.049	0.047	0.064	0.122	0.164	0.115	0.05	0.02	0.004	0.55	0.474	0.008	0.319	0.014
Fluoranthene (4)	0.819	0.51	1.034	4.191	1.097	5.76	1.638	1.463	0.064	5.723	6.656	0.221	4.509	0.249
Pyrene (4)	1.352	1.148	2.273	4.249	2.485	5.031	1.481	0.867	0.061	4.252	5.505	0.188	3.334	0.162
Benz[a]anthracene (4)	0.553	0.321	0.635	2.763	0.736	2.369	0.482	0.217	0.01	2.392	1.952	0.039	1.017	0.069
Chrysene (4)	1.317	1.415	1.768	2.233	1.588	1.39	1.904	0.46	0.018	1.856	1.529	0.017	0.696	0.026
Benz[j]fluoranthene (5)	1.333	1.082	1.456	1.498	1.081	0.606	1.256	0.219	0.003	0.953	0.588	0.002	0.365	0.008
Benz[b]fluoranthene (5)	2.412	1.957	2.632	0.555	0.393	0.213	2.271	0.396	0.005	1.723	1.058	0.004	0.652	0.015
Benz[k]fluoranthene (5)	0.761	0.647	0.825	0.611	0.535	0.197	0.574	0.072	0.005	0.313	0.18	0.007	0.087	0.015
Benz[a]pyrene (5)	0.38	0.319	0.462	0.557	0.43	0.209	0.215	0.038	0.006	0.201	0.135	0.004	0.082	0.01
Indeno[1,2,3-c,d]pyrene (6)	0.204	0.166	0.209	0.199	0.166	0.084	0.147	0.031	0.003	0.134	0.106	0.004	0.076	0.009
Dibenzo[a,h]anthracene (5)	0.042	0.029	0.042	0.04	0.027	0.01	0.027	0.004	0	0.019	0.015	0	0.01	0
Benz[g,h,i]perylene (6)	0.138	0.107	0.134	0.096	0.101	0.045	0.07	0.014	0.001	0.054	0.043	0.003	0.019	0
Total	9.567	7.983	11.859	17.443	9.018	16.404	10.383	4.013	0.287	23.923	24.259	0.886	17.514	1.028
3-ring	0.245	0.257	0.374	0.444	0.371	0.483	0.31	0.225	0.108	6.185	6.484	0.394	6.645	0.459
4-ring	4.041	3.394	5.71	13.436	5.906	14.55	5.505	3.007	0.153	14.223	15.642	0.465	9.556	0.506
5-ring	5.054	4.121	5.543	3.381	2.547	1.265	4.424	0.741	0.019	3.266	2.021	0.017	1.226	0.048
6-ring	0.342	0.273	0.343	0.295	0.267	0.129	0.217	0.045	0.004	0.188	0.149	0.007	0.095	0.009
3-ringed/Total	2.6	3.2	3.2	2.5	4.1	2.9	3	5.6	37.6	25.9	26.7	44.5	37.9	44.6
4-ringed/Total	42.2	42.5	48.1	77	65.5	88.7	53	74.9	53.3	59.5	64.5	52.5	54.6	49.2
5-ringed/Total	52.8	51.6	46.7	19.4	28.2	7.7	42.6	18.5	6.6	13.7	8.3	1.9	7	4.7
6-ringed/Total	3.6	3.4	2.9	1.7	3	0.8	2.1	1.1	1.4	0.8	0.6	0.8	0.5	0.9
Fla/(Fla + Pyr)	0.38	0.31	0.31	0.5	0.31	0.53	0.53	0.63	0.51	0.57	0.55	0.54	0.57	0.61
BaA/(BaA + Chr)	0.3	0.18	0.26	0.55	0.32	0.63	0.2	0.32	0.36	0.56	0.56	0.7	0.59	0.73
InPy/(InPy + BghiP)	0.6	0.61	0.61	0.67	0.62	0.65	0.68	0.69	0.75	0.71	0.71	0.57	0.8	1
5-ringed/3-ringed	20.63	16.04	14.82	7.61	6.87	2.62	14.27	3.29	0.18	0.53	0.31	0.04	0.18	0.1
6-ringed/3-ringed	1.4	1.06	0.92	0.66	0.72	0.27	0.7	0.2	0.04	0.03	0.02	0.02	0.01	0.02

Fla, Fluoranthene; Pyr, Pyrene; BaA, Benzo(a)anthracene; Chr, Chrysene; InPy, Indeno(1,2,3-cd) pyrene; BghiP, Benzo (g, h, i) perylene.

were observed in the coal samples from the Santanghu Basin. Results of individual macerals (vol%, mmf–mineral matter free) are given in Table 1 and Fig. 2. The vitrinite group has a content varying from 18.8 and 85.3 vol% with an average of 48.4 vol%, the most dominant maceral is collodetrinite, with an average content of 23.5 vol%. The liptinite group is not commonly observed, and its content ranges between 0.1 and 7.2 vol% with an average of 0.7 vol%. The inertinite ranges from 7.5 to 73.6 vol% with an average of 47.2 vol% with an average content of 14.8 vol% for fusinite and 18.6 vol% for semifusinite. The three dominant macerals of the inertinite group were fusinite, semifusinite and inertodetrinite, with average contents of 14.8 vol%, 18.6 vol% and 11.3 vol%, respectively.

In this study we found frequently developed macroscopical fusain in coal samples (Figs. 3 a–b), along with high contents of pyrogenic inertinite (Figs. 2 and 3). Fusinite with regularly arranged cell walls and ray cells visible in oblique and cross sections (Figs. 3 e–g). The samples were found to have clusters of secretinite, which were also significantly more reflective than the accompanying vitrinite (Fig. 3j). These microscopic features, such as the homogenization of previously stratified cell walls (Figs. 3 c–d), are consistent with the characteristics of fossil charcoal described by previous studies (Scott, 2010; Zhao et al., 2023; Shao et al., 2024).

In addition, in this study, many of the macerals in the coal are very irregular in shape and contain pores of various sizes, which are consistent with the characteristics of natural char (Fig. 4). The natural char content varies from 0 and 12.4 vol% with an average of 3.6 vol% (Fig. 2).

There was no marked difference in reflectance between the inertinite and the natural char, so they were counted together. The reflectance of inertinite and natural char ranges from 1.34 % to 2.67 % with an average of 1.92 % (Table 1). The vitrinite reflectance of the coals is on average 0.35 %, indicating a low rank coal.

4.2. PAHs compounds

A series of 2-ring to 6-ring PAHs were detected in samples from the Xishanyao Formation in the Santanghu Basin, and a total of 17 PAHs were identified (Fig. 5). The major PAHs compounds identified include 3-ringed: fluoranthene (Flu), phenanthrene (Phe), anthracene (Ant), 4-ringed: fluoranthene (Fla), pyrene (Pyr), benzo(a)anthracene (BaA), chrysene (Chr), 5-ringed: benzo(j)fluoranthene (BjF), benzo(b)fluoranthene (BbF), benzo(k)fluoranthene (BkF), benzo(a)pyrene (BaP), dibenzo(a,h)anthracene (DahA), and 6-ringed: benzo(g,h,i)perylene (BghiP), indeno(1,2,3-cd)pyrene (InPy).

The quantitative analyses of PAHs showed that the total concentration varies from 0.564 to 24.259 µg/g rock with an average of 10.204 µg/g rock in the coal samples, and 0.108 to 4.116 µg/g rock with an average of 1.376 µg/g rock in the mudstone samples, which is significantly lower than that of the coals. Among the PAHs in coal samples, the most abundant compounds were the 4- and 5- ring aromatics (average content >80 %), followed by 3-ring, 6-ring, and 2-ring aromatic compounds in descending order (Fig. 5). And in the mudstone, the most abundant compounds were the 3- and 4- ring aromatics (average content >90 %).

4.3. n-alkanes distribution

The major n-alkanes compounds identified in all samples are in the range of C₁₆ to C₃₃. The quantitative analyses of n-alkanes showed that the total concentration varied from 10.772 µg/g rock to 86.516 µg/g rock with an average of 34.144 µg/g rock in all samples. The high-molecular-weight (HMW; ≥C₂₅) n-alkanes were dominant in samples with an average of 67.4 % (Table S1).

The n-alkanes in the thick coal seams are mainly bimodal, and the mudstone is mainly dominated by long-chain n-alkanes, which are

indicative of terrestrial higher plant sources, but in the mudstone the content of the organic components is low.

5. Discussion

5.1. Evidence of palaeowildfire

5.1.1. Evidence from coal maceral

Scott (2010) considered the inertinite in coal to be equivalent to fossil charcoal, fusinite is formed by higher temperature wildfire combustion, and semifusinite is formed by lower temperature wildfire combustion. Moroeng et al. (2025) stated that the evidence suggests even degradosemifusinite is combusted first then degraded biologically, in conjunction with the conclusions of Jones et al. (1991) and Scott and Glasspool (2007), it is most probable that most semifusinites are the product of low-temperature wildfires. ICCP (2001) documented that inertodetrinite are relics from palaeowildfires in or around the peatland where the coal formed. The average percentage of the fusinite + semi-fusinite + inertodetrinite in the inertinite group is 94.5 % in the coals. The error introduced by the inclusion of a small proportion of inertinite, without a known combustion location, is thus considered comparatively negligible (Diessel, 2010; Zhou et al., 2024).

Kwiecinska and Petersen (2004) argued that natural char is formed by the influence of heat from wildfires on coal or on gelified organic

matter in peat, and the natural char may be an additional palaeoenvironmental indicator of peat fire (Xu et al., 2020; Han et al., 2024). Generally, the low heating rates and low final temperatures form denser char morphotypes, in contrast, pulverized fuel combustion chars formed at much higher temperatures generally have significantly higher porosity (Petersen, 1998; Kwiecinska and Petersen, 2004). The natural chars in samples are less porous with decreased visual original plant structures and could be consistent with gelified organic matter combustion products (Kwiecinska and Petersen, 2004), and can be used as evidence of peatland wildfires (Fig. 4).

Abundant fusain bands, high inertinite content and high natural char content indicate the frequent occurrence of local or in-situ wildfires in peat mires during the Aalenian of the Santanghu Basin (Figs. 3 and 4).

5.1.2. Evidence from PAHs

The PAH component ratios used in modern analogues to determine petrogenic (i.e., diagenetic alteration of natural biolipids and emissions of non-combustion derived diagenetic processes) vs. pyrogenic (fire) origins for PAHs have been successfully applied in palaeowildfire studies (Fox et al., 2022b). Generally, the ratio of Fla / (Fla + Pyr) > 0.5 is considered to be a typical characteristic for combustion sources, while Fla / (Fla + Pyr) < 0.4 indicates petrogenic source, and 0.4 < Fla / (Fla + Pyr) < 0.5 indicates a mixed source with combustion and petrogenic substances (Yunker et al., 2002). The ratio of BaA / (BaA + Chr) < 0.2 is

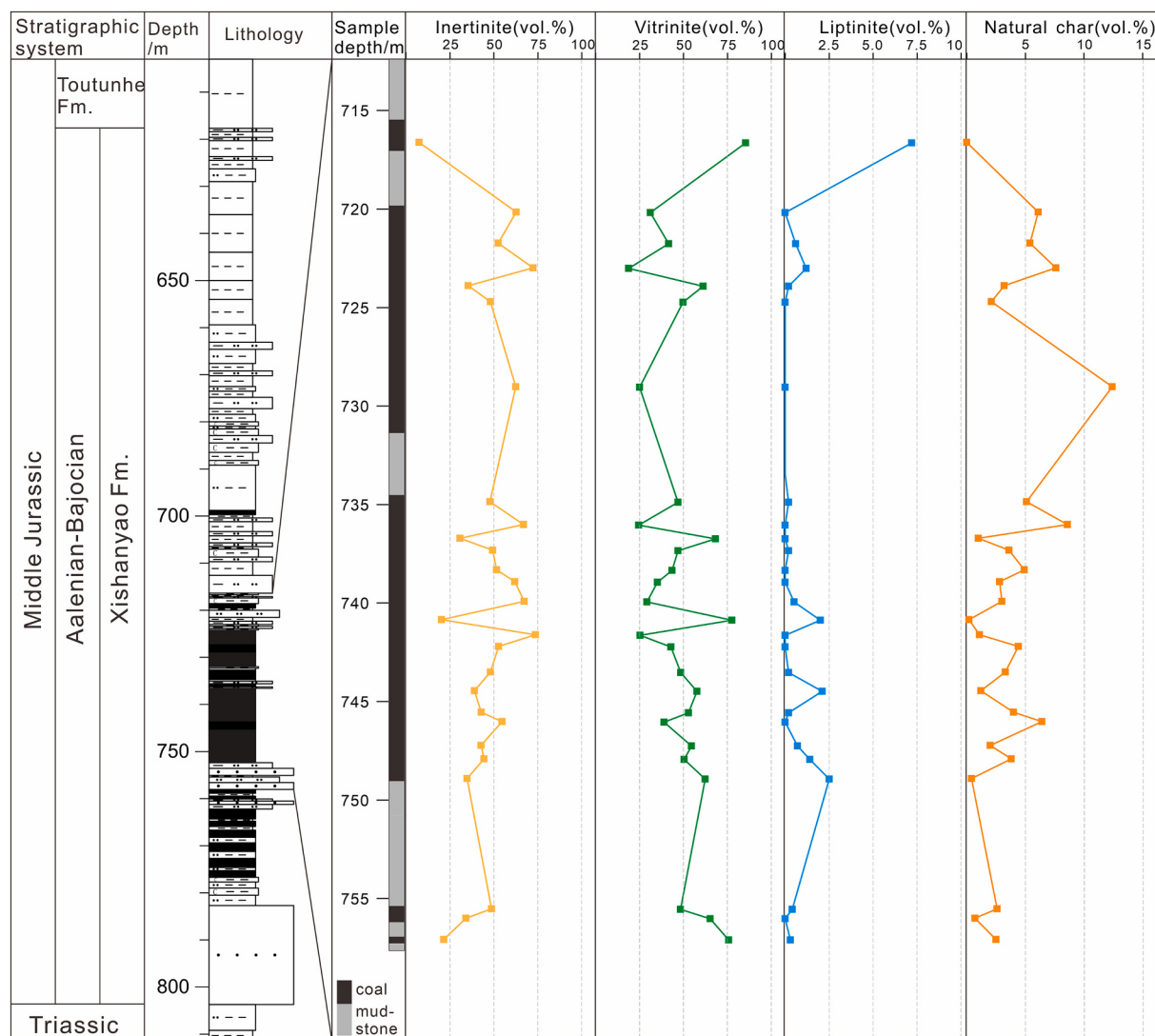


Fig. 2. Distribution of macerals and inertinite of the Tqc-1 from the Middle Jurassic Xishanyao Formation in the Santanghu Basin.

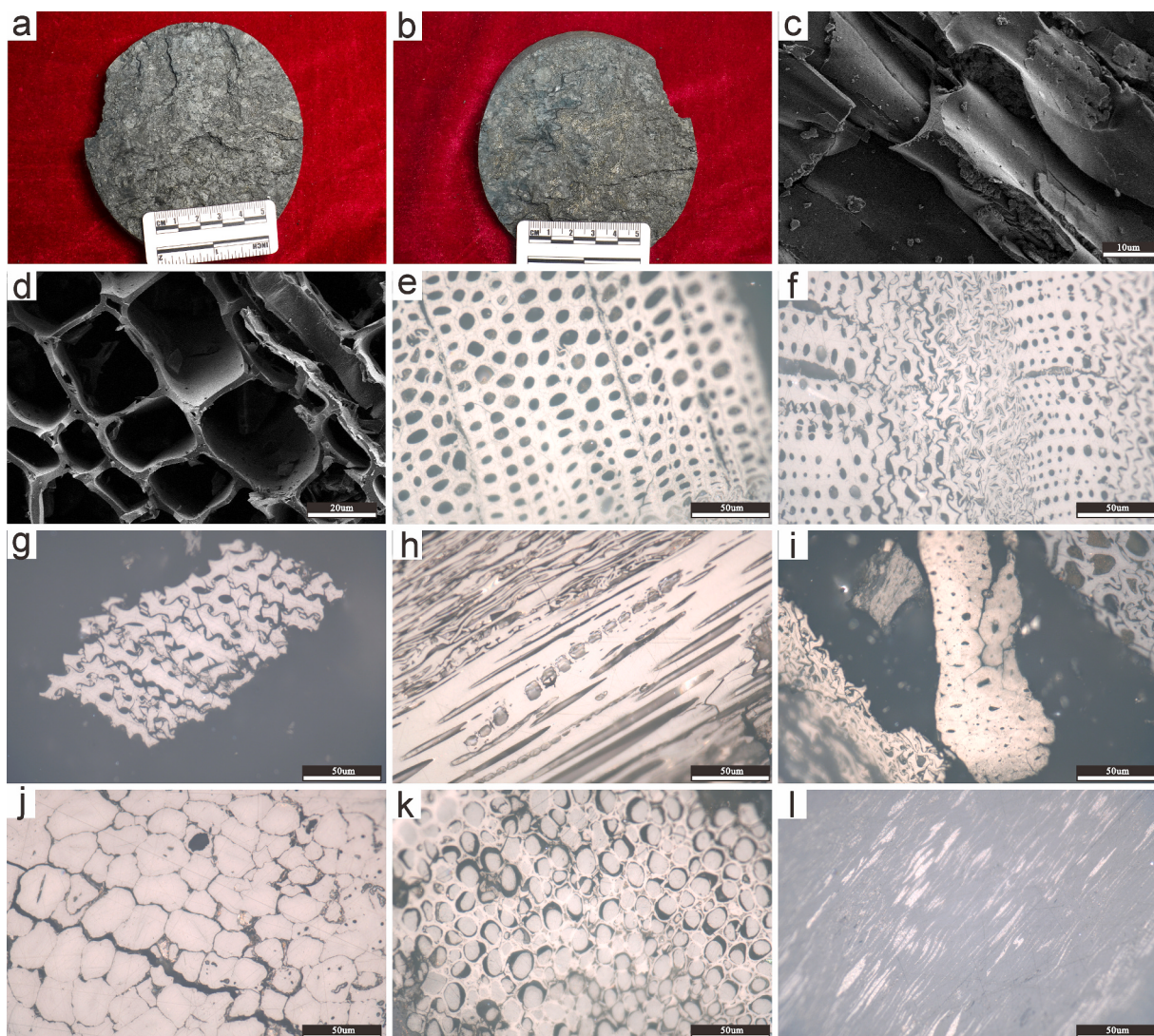


Fig. 3. Photos of fusain and inertinite from coal seam in the Middle Jurassic Xishanyao Formation of the Santanghu Basin, NW China. a–b. Photograph showing fusain is of banded distribution. c–d. Homogenization of previously stratified cell walls. e. Cross sections of fusinite clearly shows the regularly arranged cells. f–g. The cell walls of fusinite and semi fusinite are fractured and damaged during sediment compaction. h. Oblique sections of fusinite showing ray cells. i. Charred plant tissue, maybe some kind of parenchyma or simply late wood with thick cell walls. j. Clumps of secretinites. k. Fusinites are filled with gelinite. l. Micrinite fill the cellular lumen of telinite. c–d, SEM images. e–l, under reflected light with oil-immersion. Specimens: a–d, 723.09 m, e, 740.03 m, f, 736.13 m, g, 738.43 m, h, 743.62 m, i, 741.73 m, j, 745.66 m, k, 747.35 m and l, 721.84 m.

used for evidence of petrogenic origin and the ratio > 0.35 indicates a combustion origin (Yunker et al., 2002; Fox et al., 2022a). Accordingly, the ratio of InPy / (InPy + BghiP) is also used for identification of petrogenic and combustion inputs, with the ratio < 0.2 indicating a petrogenic origin and the ratio > 0.2 representing a combustion origin (Yunker et al., 2002; Fox et al., 2022a).

Recent studies have shown that Fla is more susceptible to microbial degradation than its stabler isomer Pyr, and Fla concentrations in PAHs increase with larger input of pyrogenic organic matter (Karp et al., 2018). PAHs are characterized by high Fla / (Fla + Pyr) values in most of the studied samples, and only six samples showed values < 0.4 (Table 2, Fig. 6a), probably due to the in-homogeneity of the organic matter combustion (Zhao et al., 2023). The same observation was made for BaA / (BaA + Chr) values (Fig. 6), representing a dominance of biomass burning. The InPy / (InPy + BghiP) results indicate that most of the samples are combustion sources, except for a few samples with very low levels of high PAHs (Fig. 6b). In summary, the values of Fla / (Fla + Pyr), BaA / (BaA + Chr), and InPy / (InPy + BghiP) clearly indicate the

pyrogenic origin of PAHs in the studied samples and can be used as biomarkers for palaeowildfires.

In addition to the occurrence of inertinite and natural char, the high concentration of pyrogenic PAHs preserved in the studied samples further proves the frequent occurrence of wildfires within the Middle Jurassic.

5.2. Correlation of multiple indicators of palaeowildfire

The inertinite content, natural char content and total PAHs in the samples showed a high degree of consistency in vertical variation, demonstrating their good correspondence as multiple indicators of palaeowildfire, and mutually verifying their validity as indicators of palaeowildfires.

The average reflectance of the inertinite of coal samples ranged from 1.34 % to 2.67 %, with an average of 1.94 %, corresponding to combustion temperatures of 342–498 °C, with an average combustion temperature of 412 °C (Fig. 7b) (Jones, 1997). The palaeowildfire types

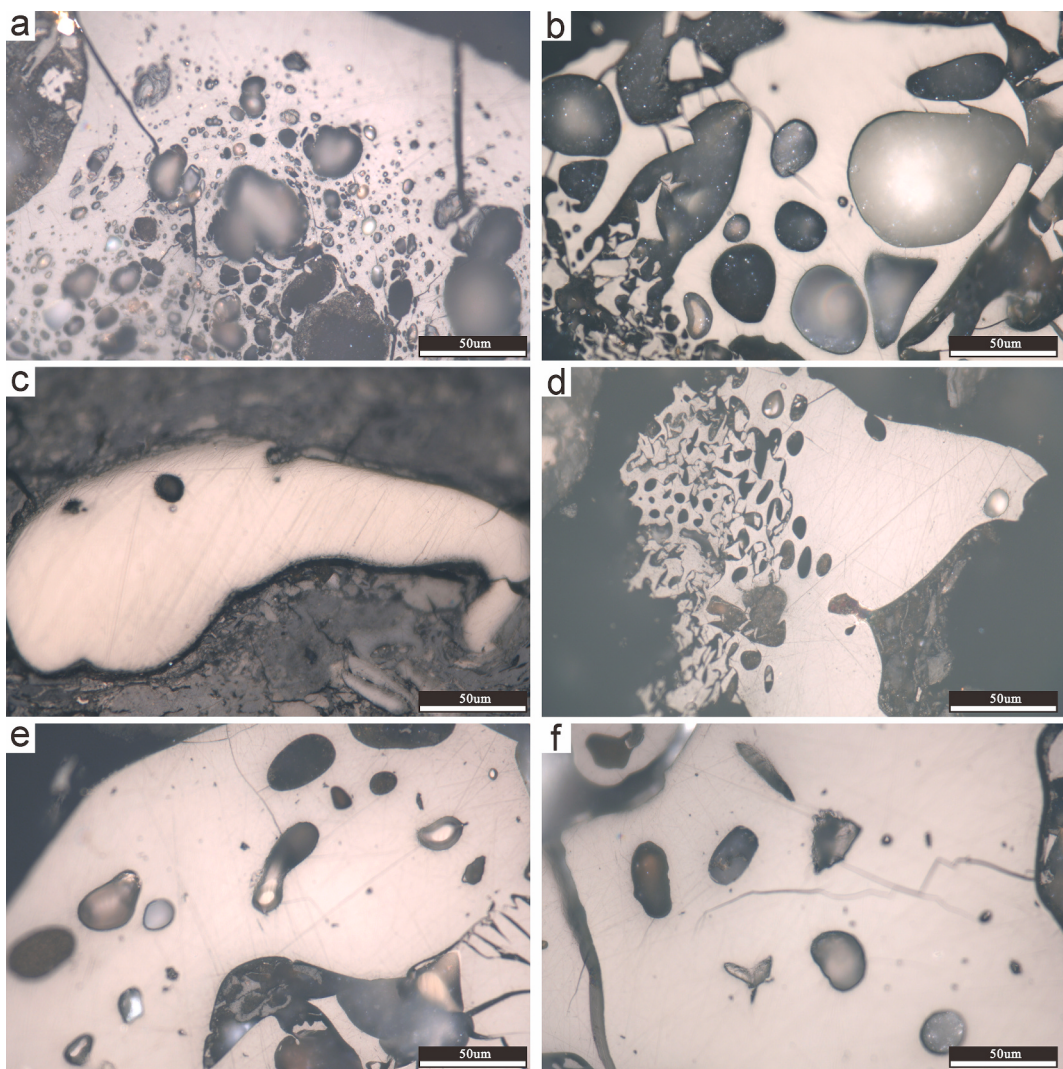


Fig. 4. Photomicrographs of natural char in the coal seam in the Middle Jurassic Xishanyao Formation from the TQC well in the Santanghu Basin, NW China. All images in reflected light under oil-immersion. a, 743.62 m, b, 721.84 m, c, 729.13 m, d, 739.03 m, e, f, 737.43 m.

recovered here are dominated by ground and surface fires, but unlike other Middle Jurassic basins in northwestern China (Xu et al., 2020; Xie et al., 2022; Zhao et al., 2023; Han et al., 2024; Zhou et al., 2024), the proportion of high-temperature crown fires has increased in this region, accounting for more than 25 % of the total in a small number of strata. Overall, the proportion of surface fire and crown fire in the upper seam (720–732 m) is higher than that in the lower seam (735–749 m), indicating greater wildfire intensity (Fig. 7a).

The ratios of 5/3- and 6/3-rings of PAHs were used in the samples to reflect palaeowildfire intensity, but the 5- and 6-ring components of the mudstones were very low, averaging less than 5 %, resulting in both ratios being close to 0. In contrast, the content of 3-ring components in the coal samples varies considerably, with contents ranging from 1.8 to 58 %. The average proportion of 3-ring components in the thicker coal seams in the 735–750 m is about 3 %, which leads to the abnormally high values of the two ratios, do not corresponding to the combustion temperatures recovered from the reflectivity of the inertinite (Fig. 8).

The reason for this may be related to the state of preservation of the samples and the environmental sensitivity of the low-ring PAH components. Samples are stored unsealed in core banks for long periods of time (two years), and the short half-life (tens, etc., of hundreds of days) of the low-ring PAHs under light and oxygen conditions may result in loss

during storage (Mackay et al., 2006). This study reaffirms the unreliability of PAH ratios of different ring numbers as a reflection of palaeowildfire intensity (Karp et al., 2020).

There is a clear correspondence between the natural char content of the samples and the variation in the proportion of ground fires, suggesting that natural charcoal is more likely to be formed from low-temperature wildfires, which is a validation of the modern experimental results by the evidence in the geological record. It should be noted that there is some natural char with high porosity in the samples (Fig. 4 a,b), indicating that a proportion of high temperature wildfires were occurring at the time, which corresponds to the relatively high content of inertodetrinitite (Table 1) (Petersen, 1998; Kwiecińska and Petersen, 2004).

The material sources of the inertodetrinitite is complex, with some of the debris possibly originating from smoke input from the crown fire, which often show high reflectance (Scott and Glasspool, 2007). Some may be transported by water, have a very large size range and these may show a range of reflectance values (Scott, 2000). Whereas plant tissues becomes fragile charcoal when it reaches charring temperatures of 300 °C and above (Jones, 1997; Li et al., 2024), some of inertodetrinitite may also be derived from fragments of incomplete combustion products (fusinite or semifusinite) deposited in situ. In the context of such a

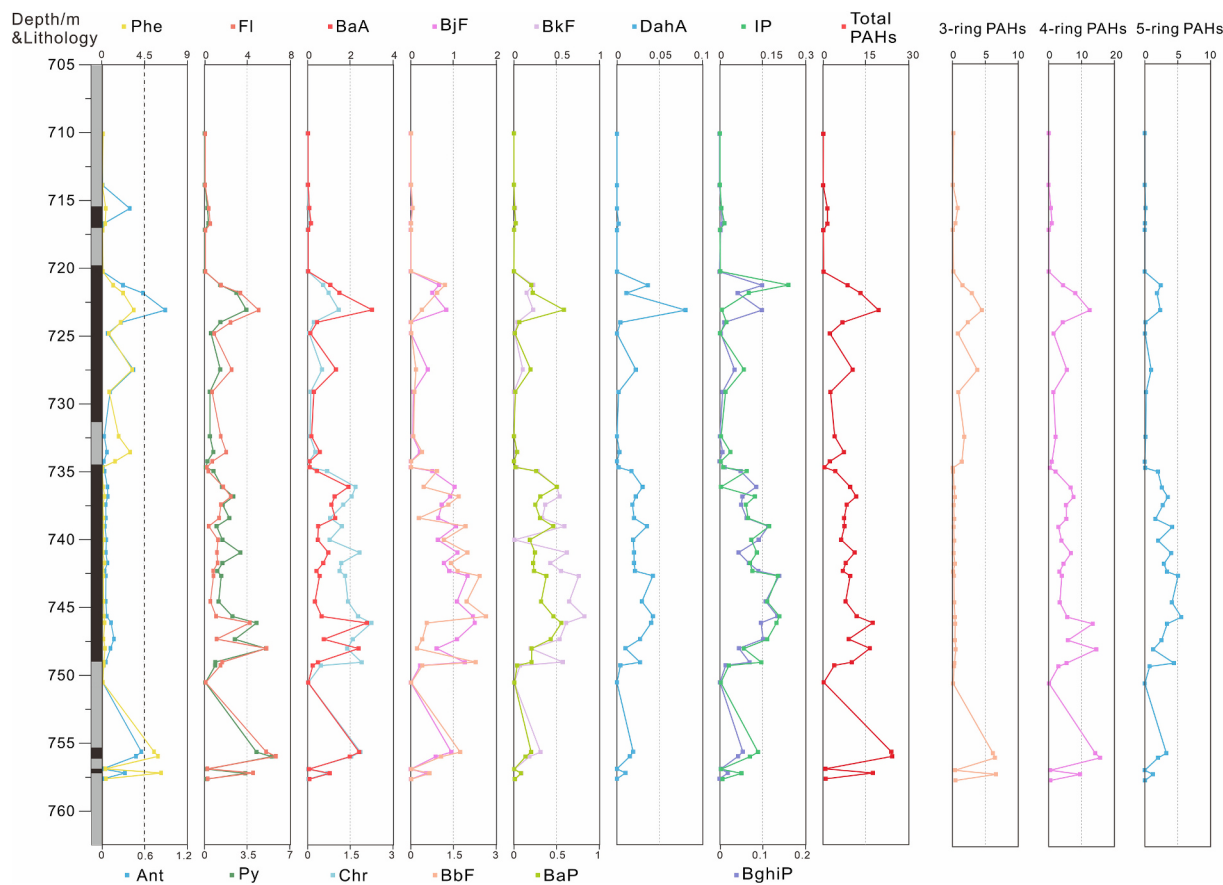


Fig. 5. Contents of selected PAHs of the Middle Jurassic Xishanyao Formation in the Santanghu Basin, NW China. PAHs content is in ug/g rock.

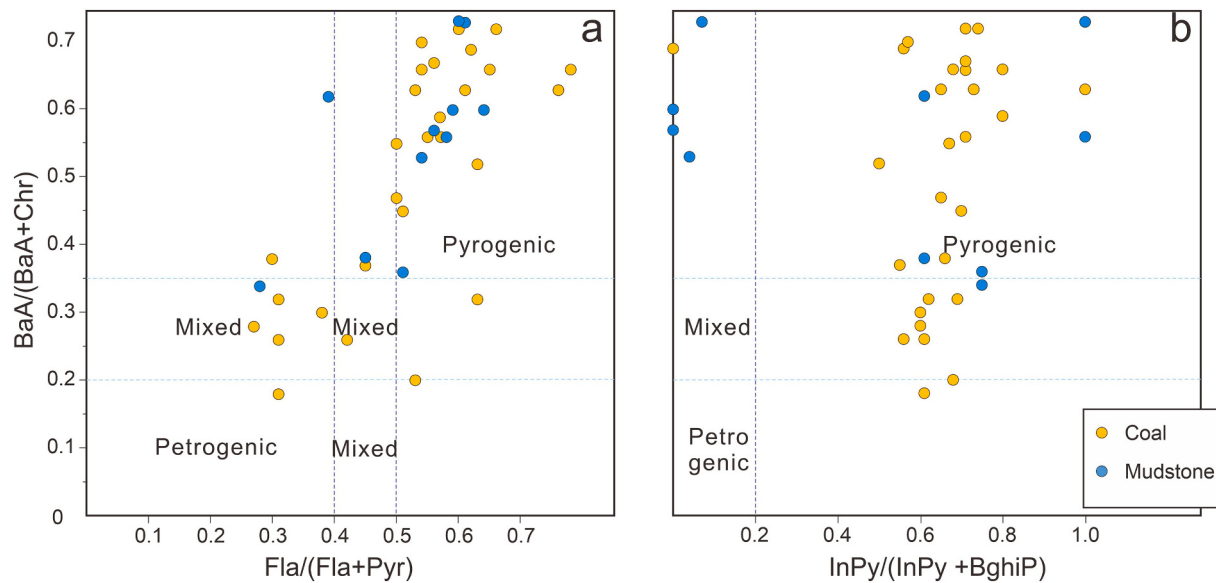


Fig. 6. Plots of PAH parameters that indicate origins of PAHs in the Middle Jurassic Xishanyao Formation from the Santanghu Basin, NW China.

complex source, the potential use of inertodetrinite in determining peat palaeoenvironment is therefore limited (Scott and Glasspool, 2007). The inertodetrinite with small particles and high-reflectance may be representing crown fire in the studied samples (Scott, 2010; Zhao et al., 2023), instead of a high content of inertodetrinite indicating a high proportion of crown fire.

5.3. Palaeobotany and palaeoclimate characteristics

5.3.1. Palaeobotanical characteristics

The flora of the Mesozoic was dominated by ‘filicalean’ ferns and gymnosperms (Cycadopsida, Ginkgopsida, Czechanowskiales and Coniferopsida), with both Cycadopsida and Ginkgopsida reaching their peak during the Jurassic (Vakhrameev, 1991). Ginkgo fossils are generally

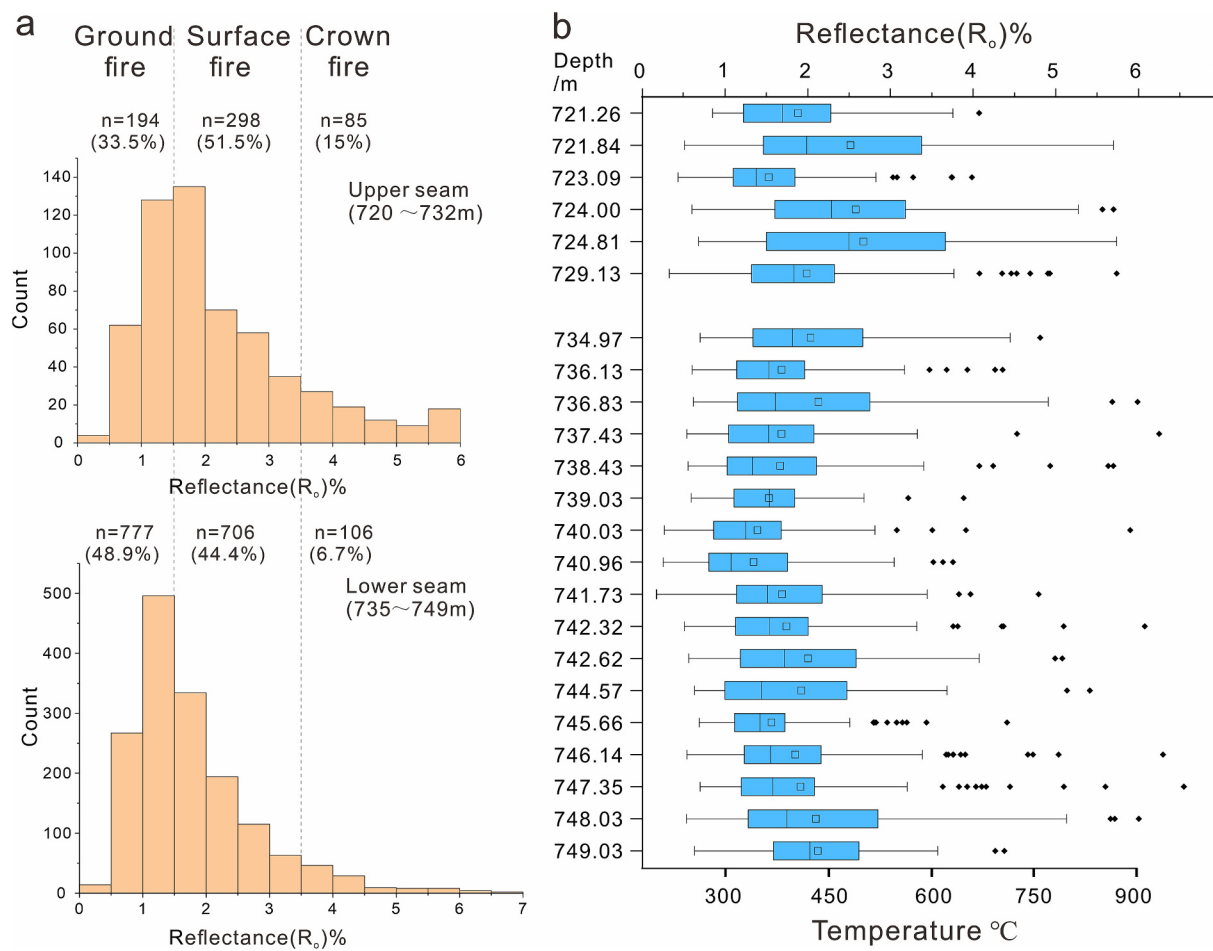


Fig. 7. a. Sum of inertinite reflectance histograms and the proportion of wildfire types; b. Box plots in the Middle Jurassic Xishanyao Formation from the Santanghu Basin, NW China.

preserved in dark sandstone and mudstone, and they are most commonly and abundantly found in coal-bearing strata, indicating that Ginkgo was one of the important coal-forming plants of the Jurassic period (Wang et al., 1997; Deng, 2007). Sometimes Ginkgo fossils can be seen distributed in large numbers along the surface, showing the characteristic of seasonal leaf fall (Wang et al., 1997).

By studying the samples from the Xixiagou area in the Santanghu Basin (Fig. 1b), Huang (2002) pointed out that the average content of gymnosperm pollen in the Xishanyao Formation was 57 %, and the average content of fern spores was 42 %, with the highest abundance of *Osmundacidites* of the Osmundaceae, followed by *Cyathidites* and *Deltoidospora* of the Cyatheaceae, and the bryophyte fossils could be as high as 10.8 % in individual samples. By studying samples from the Tiaohu Depression in the Santanghu Basin (Fig. 1b), Yang et al. (2024) suggested that the gymnosperm pollen content of the Xishanyao Formation ranged from 12.8 to 87.6 %, with an average of 53.5 %, and was slightly higher than that of fern spores, which ranged from 12.4 to 87.2 %, with an average content of 46.4 %.

Spores and pollen, as the reproductive organ of plants, provide insight into the plant taxa of the Aalenian–Bajocian period in the Santanghu Basin through the analysis of their parent plants (Huang, 2002; Yang et al., 2024). The ecology of the various groups of parent plants mentioned is mainly based on published palaeoecological information and partly on comparison with extant relatives of the plant groups (nearest living relatives) (Abbink et al., 2004). Following the classification scheme of Abbink et al. (2004), we can probably reconstruct the distribution characteristics of Middle Jurassic plant communities within

the study area.

The alpine zone is a dense forest, dominated by large evergreen trees of Pinaceae and Cupressaceae, accompanied by Ginkgoaceae, Cycadaceae and Taxodiaceae, etc. The undergrowth consists mainly of small ferns such as *Lycopodium*. On the sunny slopes and flat land, various ferns such as *Osmundaceae* grow. Algae and *Equisetales* grow in the water, and Fontinalaceae and Equisetales are common in the swampy areas around the lake, while large tree ferns such as Cyatheaceae grow near the water body (Huang, 2002; Abbink et al., 2004; Deng, 2007; Yang et al., 2024).

5.3.2. Palaeoclimatic characteristics

Belcher and McElwain (2008) suggested that the lower pO₂ limit for combustion should be 15 %, but for the wildfire to widely spread required pO₂ 18.5 % (Belcher et al., 2010). The atmospheric oxygen level during the Middle Jurassic, calculated from databases in Zhou et al. (2024), was about 26 %, which was enough to support the occurrence and spread of wildfires. In fact, the elevated pO₂ would promote and sustain more fires compared to our modern levels of 21 %. In the presence of sufficient atmospheric oxygen, other factors may turn out to be critical to the control of wildfire regimes, mainly climate and vegetation (Baker et al., 2019).

The atmospheric carbon dioxide levels in the Middle Jurassic reached more than 1000 ppm (Wu et al., 2016; Foster et al., 2017), and average surface temperatures reached about 19 °C, which was 5–10 °C higher than today (Li et al., 2022b). Zhang et al. (2023) reconstructed palaeoclimate of the early Middle Jurassic in Santanghu basin through a

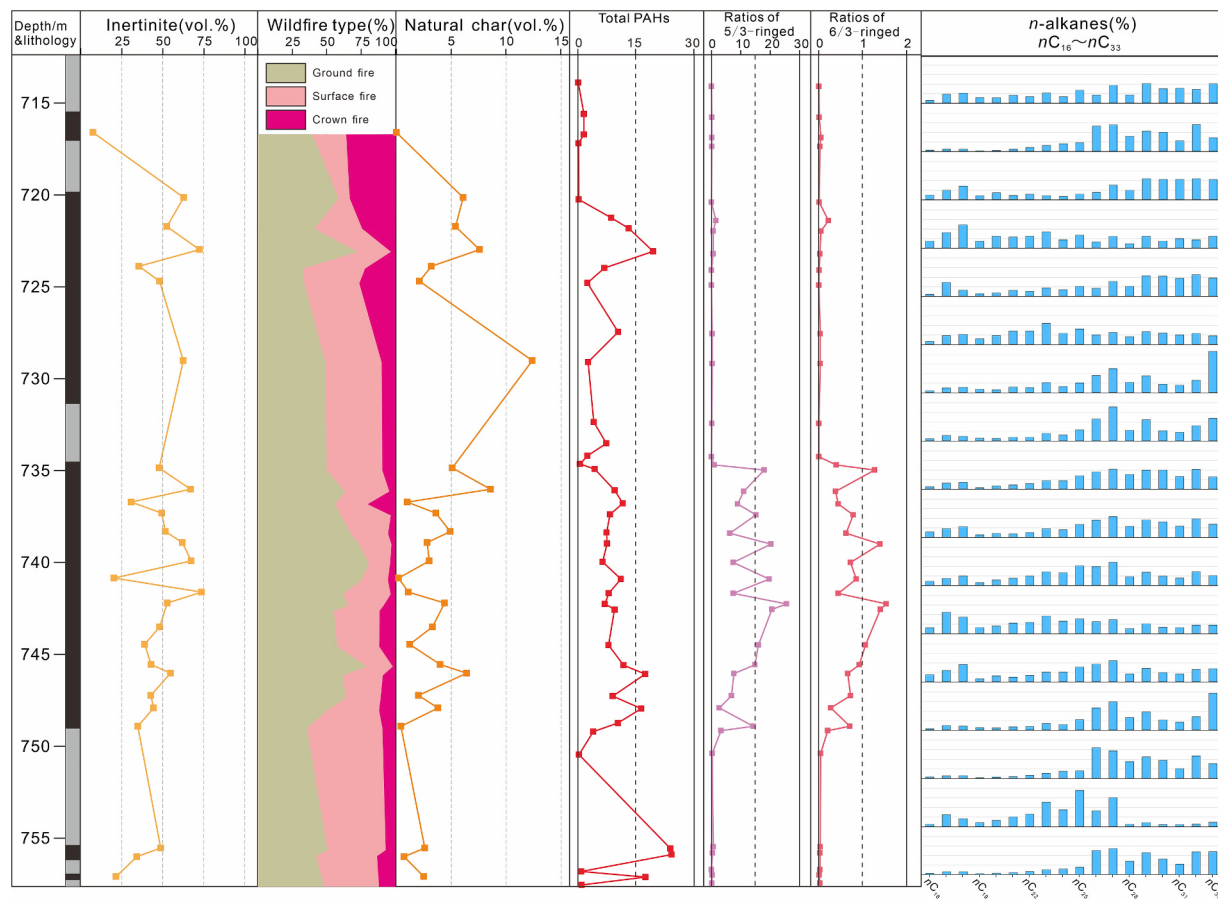


Fig. 8. Plots of multiple palaeowildfire indicators and *n*-alkanes in the Middle Jurassic Xishanyao Formation, Santanghu Basin, NW China.

variety of chemical weathering and climate indicators, revealing a hot and humid climate condition with shifted from wet to dry. Du et al. (2024) reconstructed the palaeoclimate of the Middle Jurassic in the adjacent Tuha Basin, indicating that the palaeoclimate was warm and humid, correlating with the intensification of the East Asian monsoon circulation. Zhou et al. (2024) quantified the palaeoclimate of the Middle Jurassic in northwestern China, which can be divided reference to Köppen climate classification scheme into a Monsoon-influenced hot-summer humid continental climate (climate symbol: Dwa) (Kottke et al., 2006; Peel et al., 2007). Palaeoflora characteristics (Deng et al., 2017) and palaeoclimate databases (Li et al., 2022b) also indicate a palaeoclimate with four distinct seasons in northwestern China during the Middle Jurassic.

5.3.3. Feedback mechanisms between factors in palaeoecosystems

The vast majority of Middle Jurassic land plants were C₃ species (Sage, 2004), which were more sensitive to high levels of CO₂ than C₄ plants, therefore photosynthesis in the C₃ plants during the Jurassic was more responsive to elevated CO₂ (Ainsworth and Long, 2005). Therefore, high CO₂ concentrations, warm climate and seasonal precipitation in the Jurassic contributed to terrestrial plants flourishing, that in turn may have provided increased amounts of fuel for palaeowildfires (Zhong et al., 2003; Deng, 2007; Zhang et al., 2020; Zhao et al., 2023).

Biological studies of modern forest wildfires have shown that frequent and low-severity wildfires can be necessary to maintain species diversity in forests, rather than destroying plant populations (Kroll et al., 2023). The major Jurassic plant groups are believed to had their own characteristics to defend against or adapt to low-severity palaeowildfires (Korasidis et al., 2019; Van Konijnenburg-Van Cittert, 2002). The

persistence of high inertinite content in the thick coal seams of the study area suggests that this feedback mechanism may have existed in Jurassic as well.

Frequent climate fluctuations in the Jurassic (Scotese et al., 2021; Judd et al., 2024) and the contrasting seasons during the Middle Jurassic (Li et al., 2022b) may have allowed mires to temporarily dry out so that the uppermost part, above the water table, could have been affected by surface fires (Zhou et al., 2024). Natural char is evidence of the existence of wildfires in such peatlands (Fig. 4), and due to the high plant productivity (Ainsworth and Long, 2005), recently dead plants may also be turned into fuel for wildfires (Scott, 2000). This may result in large differences in the content of inertinite groups in the same coal seam (Fig. 7).

The *n*-alkanes in the two thick coal seams were dominated by bimodal types with a clear odd/even predominance (Fig. 8). The lower seam (735–749 m) has a high percentage of short- and medium-chain *n*-alkanes, whereas the upper seam (720–732 m) is dominated by long-chain (Fig. 8). This indicates that there may have been a relatively high abundance of aquatic plants and algae (Liu et al., 2022b). Modern research as well as evidence from the geological record suggests that wildfire activity can result in the transport of phosphorus to water bodies, leading to eutrophication and the growth of aquatic plants (Mahowald et al., 2008; Liu et al., 2022a; Xu et al., 2022).

Multiple wildfire indicators in the samples of Santanghu basin are evidence of frequent wildfires at that time (Fig. 8). The sections have relatively more short- and medium-chain *n*-alkanes, so the mechanism by which wildfires lead to an increase in aquatic plants may also be present in the Jurassic (Figs. 8 and 9). It should be noted that the upper seam (720–732 m) exhibits a clearly higher proportion of surface fire

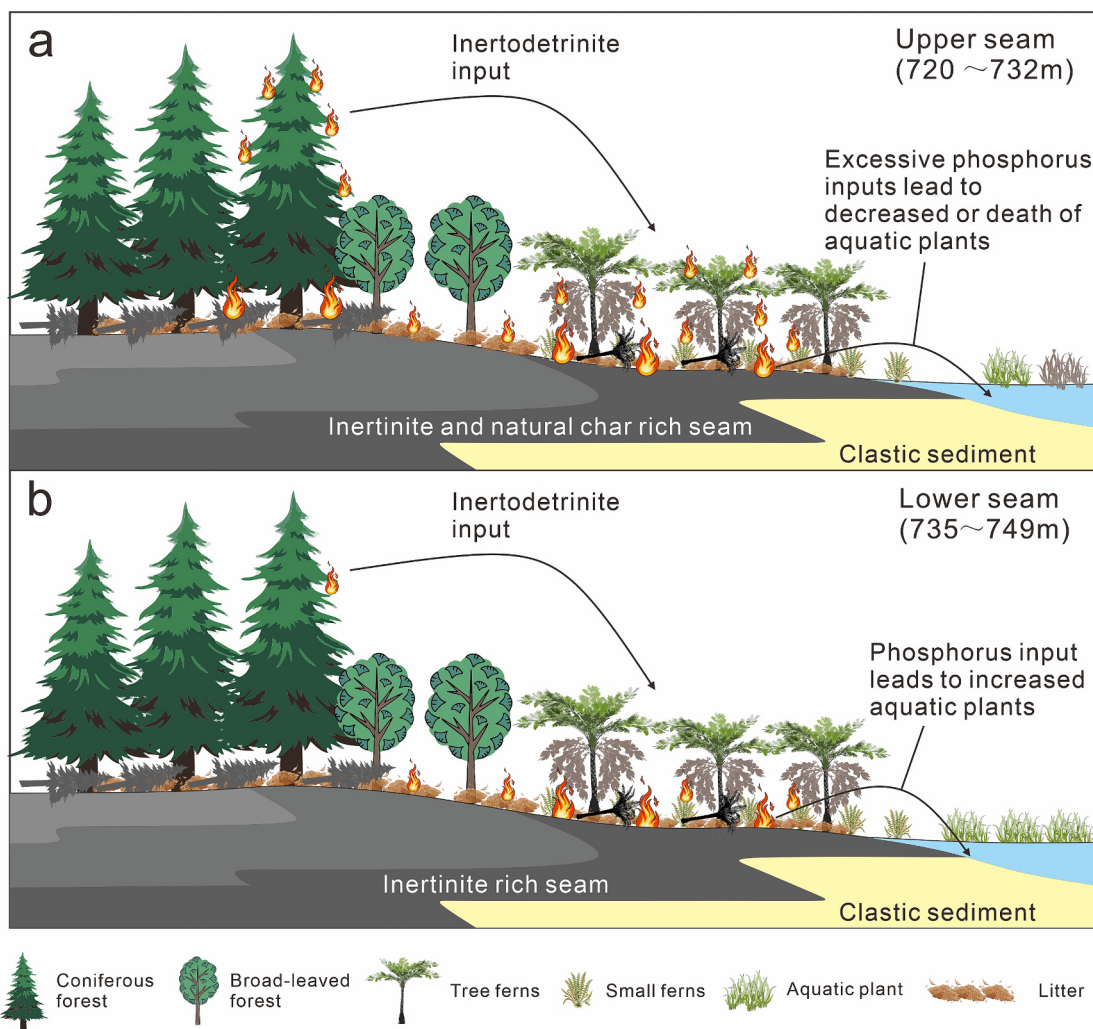


Fig. 9. Schematic model illustrating possible relationship between palaeowildfire and palaeobotany in the Middle Jurassic Xishanyao Formation of the Santanghu Basin, NW China.

and crown fire than the lower seam (735–749 m) (Fig. 7), the upper coal seam exhibits a reduction in the medium-chain *n*-alkanes, while the short-chain *n*-alkanes also decreases in strata characterized by high proportions of high-temperature fires (Fig. 8). This indicates that increased wildfire activity may lead to excessive phosphorus inputs into water bodies, resulting in the reduction or even death of aquatic plants (Fig. 9). In severe cases, this could cause oxygen depletion in water bodies, triggering anoxic events (Xu et al., 2022).

6. Conclusion

- (1) There is a consistent pattern between the trends of inertinite content, natural char content and PAHs. All this evidence suggests that palaeowildfires were frequent during the Aalenian in the Santanghu Basin. The main types of palaeowildfires were lower temperature ground and surface fires, with the high temperature crown fire occurred occasionally.
- (2) Inertinite and natural char can be used as reliable coal petrological evidence for palaeowildfires. Low-ring PAHs are extremely unstable and therefore the ratios of high to low rings are unlikely to be reliable indicators of palaeowildfire intensity.
- (3) Palaeoclimate was the main driver, palaeobotanic vegetation provided the fuel, and palaeowildfires were the mechanism of preservation during the formation of the inertinite-rich coals.

There is also a possible positive effect of palaeowildfires on aquatic plants.

CRediT authorship contribution statement

Jiamin Zhou: Writing – original draft, Visualization, Software, Methodology. **Longyi Shao:** Writing – review & editing, Resources, Funding acquisition. **Timothy P. Jones:** Writing – review & editing, Methodology. **Yangyang Huang:** Validation, Software. **Mengran Chen:** Visualization, Conceptualization. **Yuedong Ma:** Visualization, Methodology. **Jing Lu:** Writing – review & editing, Supervision.

Declaration of competing interest

The authors declare that they have no known competing financial interests or personal relationships that could have appeared to influence the work reported in this paper.

Acknowledgements

This study was supported by the Key Project of the National Natural Science Foundation of China (Grant No. 42530208), the Science Fund for Creative Research Groups of the National Natural Science Foundation of China (Grant No. 42321002) and the National Natural Science Foundation of China (Grant No. 42475113).

Appendix A. Supplementary data

Supplementary data to this article can be found online at <https://doi.org/10.1016/j.palaeo.2025.113260>.

Data availability

The authors confirm that all data necessary for supporting the scientific findings of this paper have been provided.

References

- Abbingk, O.A., Van Konijnenburg-Van Cittert, J.H.A., Visscher, H., 2004. A sporomorph ecogroup model for the Northwest European Jurassic - Lower Cretaceous: concepts and framework. *Neth. J. Geosci.* 83 (1), 17–31.
- Ainsworth, E.A., Long, S.P., 2005. What have we learned from 15 years of free-air CO₂ enrichment (FACE)?: a meta-analytic review of the responses of photosynthesis, canopy properties and plant production to rising CO₂. *New Phytol.* 165 (2), 351–371.
- Allegré, C.J., Courtillot, V., Tapponnier, P., Hirn, A., Mattauer, M., Coulon, C., Jaeger, J.J., Achache, J., Schärer, U., Marcoux, J., Burg, J.P., Girardeau, J., Armijo, R., Gariépy, C., Göpel, C., Tindong, L., Xuchang, X., Chenfa, C., Guangqin, L., Baoyu, L., Jiwen, T., Naiwen, W., Guoming, C., Tonglin, H., Xibin, W., Wanming, D., Huabin, S., Yougong, C., Ji, Z., Hongrong, Q., Peisheng, B., Songchan, W., Bixiang, W., Yaoxiu, Z., Xu, R., 1984. Structure and evolution of the Himalaya-Tibet orogenic belt. *Nature* 307 (5946), 17–22.
- Baker, S.J., 2021. Fossil evidence that increased wildfire activity occurs in tandem with periods of global warming in Earth's past. *Earth Sci. Rev.* 224, 103871.
- Baker, S.J., Hesselbo, S.P., Lenton, T.M., Duarte, L.V., Belcher, C.M., 2017. Charcoal evidence that rising atmospheric oxygen terminated Early Jurassic Ocean anoxia. *Nat. Commun.* 8, 15018.
- Baker, S.J., Belcher, C.M., Barclay, R.S., Hesselbo, S.P., Laurin, J., Sageman, B.B., 2019. CO₂-induced climate forcing on the fire record during the initiation of Cretaceous oceanic anoxic event 2. *Geol. Soc. Am. Bull.* 132 (1–2), 321–333.
- Belcher, C.M., McElwain, J.C., 2008. Limits for combustion in low O₂ redefine paleoatmospheric predictions for the Mesozoic. *Science* 321 (5893), 1197–1200.
- Belcher, C.M., Mander, L., Rein, G., Jervis, F.X., Haworth, M., Hesselbo, S.P., Glasspool, I.J., McElwain, J.C., 2010. Increased fire activity at the Triassic/Jurassic boundary in Greenland due to climate-driven floral change. *Nat. Geosci.* 3 (6), 426–429.
- Castañeda, I.S., Schouten, S., 2011. A review of molecular organic proxies for examining modern and ancient lacustrine environments. *Quat. Sci. Rev.* 30 (21), 2851–2891.
- Dai, S., Liu, J., Ward, C.R., Hower, J.C., Xie, P., Jiang, Y., Hood, M.M., O'Keefe, J.M.K., Song, H., 2015. Petrological, geochemical, and mineralogical compositions of the low-Ge coals from the Shengli Coalfield, China: a comparative study with Ge-rich coals and a formation model for coal-hosted Ge ore deposit. *Ore Geol. Rev.* 71, 318–349.
- Dai, S., Bechtel, A., Eble, C.F., Flores, R.M., French, D., Graham, I.T., Hood, M.M., Hower, J.C., Korasidis, V.A., Moore, T.A., Püttmann, W., Wei, Q., Zhao, L., O'Keefe, J.M.K., 2020. Recognition of peat depositional environments in coal: a review. *Int. J. Coal Geol.* 219, 103383.
- Deng, S., 2007. Palaeoclimatic implications of main fossil plants of the Mesozoic. *J. Palaeogeogr.-English* 9 (6), 559–574.
- Deng, S., Lu, Y., Zhao, Y., Fan, R., Wang, Y., Yang, X., Li, X., Sun, B., 2017. The Jurassic palaeoclimate regionalization and evolution of China. *Earth Science Frontiers* 24 (01), 106–142.
- Diessel, C.F.K., 2010. The stratigraphic distribution of inertinite. *Int. J. Coal Geol.* 81 (4), 251–268.
- Du, Z., Wu, H., Ban, S., Cao, H., Hao, A., Ma, J., Wei, G., 2024. Geochemical and palynological records of the Early-Middle Jurassic in the Turpan-Hami Basin, NW China: Implications for paleoenvironment and paleoclimate change. *Geol. J.* 59 (6), 1724–1742. <https://doi.org/10.1002/gj.4965>.
- Feng, S., He, J., Wu, B., Lu, X., Li, W., Zhang, Y., 2018. Sedimentary characteristics and coal accumulation law of coal bearing strata in Xishanyao Formation of Santanghu Coalfield. *Coal Sci. Tech.* 45 (2), 42–55 (in Chinese with English abstract).
- Feng, S., He, J., Tian, J., Lu, X., Yang, B., 2019. The characteristic and evolution of coal-forming swamp in Hanshuiquan district, Santanghu Coalfield, Xinjiang, NW China, during the Middle Jurassic: evidence from coal petrography, coal facies and sporopollen. *Int. J. Coal Sci. Technol.* 6 (1), 1–14.
- Ficken, K.J., Li, B., Swain, D.L., Eglington, G., 2000. An n-alkane proxy for the sedimentary input of submerged/floating freshwater aquatic macrophytes. *Org. Geochem.* 31 (7–8), 745–749.
- Foster, G.L., Royer, D.L., Lunt, D.J., 2017. Future climate forcing potentially without precedent in the last 420 million years. *Nat. Commun.* 8, 14845.
- Fox, C.P., Holman, A.I., Rigo, M., Al Suwaidi, A., Grice, K., 2022a. Paleowildfire at the end-Triassic mass extinction: Smoke or fire? *Global Planet. Change* 218, 103974.
- Fox, C.P., Whiteside, J.H., Olsen, P.E., Grice, K., 2022b. Flame out! End-Triassic mass extinction polycyclic aromatic hydrocarbons reflect more than just fire. *Earth Planet. Sci. Lett.* 584, 117418.
- Gou, X.D., Wei, H.B., Guo, Y., Yang, S.L., Feng, Z., 2021. Leaf phenology, paleoclimatic and paleoenvironmental insights derived from an *Agathoxylon* stem from the Middle Jurassic of Xinjiang, Northwest China. *Rev. Palaeobot. Palynol.* 289, 104416.
- Han, Q., Liu, J., Hower, J.C., Moore, T.A., Shang, N., Zhao, S., Jia, R., Dai, S., 2024. Fire activities and their impacts on local ecosystems in the southern Ordos Basin during the Middle Jurassic: evidence from pyrogenic PAHs and petrography of inertinite-rich coal. *Palaeogeogr. Palaeoclimatol. Palaeoecol.* 636, 111972.
- Hendrix, M.S., Graham, S.A., Carroll, A.R., Sobel, E.R., McKnight, C.L., Schulein, B.J., Wang, Z., 1992. Sedimentary record and climatic implications of recurrent deformation in the Tian Shan: evidence from Mesozoic strata of the North Tarim, south Junggar, and Turpan basins, Northwest China. *Geol. Soc. Am. Bull.* 104 (1), 53–79.
- Hollaar, T.P., Baker, S.J., Hesselbo, S.P., Deconinck, J.-F., Mander, L., Ruhl, M., Belcher, C.M., 2021. Wildfire activity enhanced during phases of maximum orbital eccentricity and precessional forcing in the Early Jurassic. *Commun. Earth Environ.* 2 (1), 247.
- Hou, H., Shao, L., Liang, G., Tang, Y., Zhang, H., Zhang, J., 2022. Repeated wildfires in the Middle Jurassic Xishanyao Formation (Aalenian and Bajocian Ages) in Northwestern China. *Acta Geol. Sin-Engl* 96 (5), 1752–1763.
- Huang, P., 2002. Middle Jurassic sporopollen assemblages from Tangqian-3 well of the Santanghu Basin, Xinjiang. *Acta Micropalaeontol. Sin.* 19 (2), 178–192 (in Chinese with English abstract).
- Huang, P., 2003. A sporo-pollen assemblage from the Middle Jurassic Xishanyao Formation of the Kuisu coal-mine in the Santanghu Basin, Xinjiang. *Acta Micropalaeontol. Sin.* 20 (4), 425–434 (in Chinese with English abstract).
- ICCP, 2001. The new inertinite classification (ICCP System 1994). *Fuel* 80 (4), 459–471.
- ISO, 2009a. Methods for the Petrographic Analysis of Coals: Part 2. Method of Preparing Coal Samples.
- ISO, 2009b. Methods for the Petrographic Analysis of Coals: Part 5. Method of Determining Microscopically the Reflectance of Vitrinite.
- Jones, T.P., 1997. Fusain in late Jurassic sediments from the Witch Ground Graben, North Sea, UK. In: Mededelingen Nederlands Instituut voor Toegepaste Geowetenschappen TNO, 58, pp. 93–103.
- Jones, T.P., Scott, A.C., Cope, M., 1991. Reflectance measurements and the temperature of formation of modern charcoals and implications for studies of fusain. *Bull. Soc. Geol. Fr.* 162 (2), 193–200.
- Jones, M.W., Kelley, D.I., Burton, C.A., Di Giuseppe, F., Barbosa, M.L.F., Brambleby, E., Hartley, A.J., Lombardi, A., Mataveli, G., McNorton, J.R., Spuler, F.R., Wessel, J.B., Abatzoglou, J.T., Anderson, L.O., Andela, N., Archibald, S., Armenteras, D., Burke, E., Carmenta, R., Chuvieco, E., Clarke, H., Doerr, S.H., Fernandes, P.M., Giglio, L., Hamilton, D.S., Hanton, S., Harris, S., Jain, P., Kolden, C.A., Kurvits, T., Lampe, S., Meier, S., New, S., Parrington, M., Perron, M.M.G., Qu, Y.Q., Ribeiro, N.S., Saharjo, B.H., San-Miguel-Ayanz, J., Shuman, J.K., Tanripat, V., van der Werf, G.R., Veraverbeke, S., Xanthopoulos, G., 2024. State of wildfires 2023–2024. *Earth Syst. Sci. Data* 16 (8), 3601–3685.
- Judd, E.J., Tierney, J.E., Lunt, D.J., Montañez, I.P., Huber, B.T., Wing, S.L., Valdes, P.J., 2024. A 485-million-year history of Earth's surface temperature. *Science* 385 (6715), eadk3705.
- Karp, A., Behrensmeyer, A., Freeman, K., 2018. Grassland fire ecology has roots in the late Miocene. *Proc. Natl. Acad. Sci.* 115, 12130–12135.
- Karp, A.T., Holman, A.I., Hopper, P., Grice, K., Freeman, K.H., 2020. Fire distinguishes: Refined interpretations of polycyclic aromatic hydrocarbons for paleo-applications. *Geochim. Cosmochim. Acta* 289, 93–113.
- Korasidis, V.A., Wallace, M.W., Wagstaff, B.E., Hill, R.S., 2019. Evidence of fire in Australian Cenozoic rainforests. *Palaeogeogr. Palaeoclimatol. Palaeoecol.* 516, 35–43.
- Kottek, M., Grieser, J., Beck, C., Rudolf, B., Rubel, F., 2006. World map of the Koppen-Geiger climate classification updated. *Meteorol. Z.* 15 (3), 259–263.
- Kroll, A.J., Greenler, S.M., Dunn, C.J., Johnston, J.D., Reilly, M.J., Merschel, A.G., Hagmann, R.K., Bailey, J.D., 2023. Too hot, too cold, or just right: can wildfire restore dry forests of the interior Pacific Northwest? *PloS One* 18 (2), e0281927.
- Kwiecińska, B., Petersen, H.I., 2004. Graphite, semi-graphite, natural coke, and natural char classification - ICCP system. *Int. J. Coal Geol.* 57 (2), 99–116.
- Li, D., 1995. Hydrocarbon occurrences in the petroliferous basins of western China. *Mar. Pet. Geol.* 12 (1), 26–34.
- Li, Y., Zhao, F., 2015. Jurassic Coal Accumulation Regularity in Major Coal-Bearing Basins of Eastern Xinjiang. Science Press, Beijing, p. 237 (in Chinese).
- Li, J., Lv, L., Wang, R., Long, H., Yang, X., 2022a. Spatial distribution of n-alkanes in the catchment and sediments of Lake Lugu, Southwest China: Implications for palaeoenvironment reconstruction. *Palaeogeogr. Palaeoclimatol. Palaeoecol.* 592, 110895.
- Li, X., Hu, Y., Guo, J., Lan, J., Lin, Q., Bao, X., Yuan, S., Wei, M., Li, Z., Man, K., Yin, Z., Han, J., Zhang, J., Zhu, C., Zhao, Z., Liu, Y., Yang, J., Nie, J., 2022b. A high-resolution climate simulation dataset for the past 540 million years. *Sci. Data* 9 (1), 371.
- Li, G., Gao, L., Liu, F., Qiu, M., Dong, G., 2024. Quantitative studies on charcoalification: Physical and chemical changes of charring wood. *Fundamental Research* 4 (1), 113–122.
- Lima, A.L.C., Farrington, J.W., Reddy, C.M., 2005. Combustion-derived polycyclic aromatic hydrocarbons in the environment—a review. *Environ. Forensic* 6 (2), 109–131.
- Liu, X., Zheng, J., Yang, X., Liu, Y., 2010. Paleozoic structural evolution of Santanghu Basin and its surrounding and prototype basin recovery. *Nat. Gas Geosci.* 21 (6), 947–954 (in Chinese with English abstract).
- Liu, S., Ma, X., Zhou, J., Zhang, J., Fan, L., 2017. Xinjiang Santanghu Basin coal division of tectonic units and tectonic characteristics. *Geol. Rev.* 63 (S1), 271–272 (in Chinese with English abstract).

- Liu, D., Zhou, C., Keesing, J.K., Serrano, O., Werner, A., Fang, Y., Chen, Y., Masque, P., Kinloch, J., Sadekov, A., Du, Y., 2022a. Wildfires enhance phytoplankton production in tropical oceans. *Nat. Commun.* 13 (1), 1348.
- Liu, J., Zhao, J., He, D., Huang, X., Jiang, C., Yan, H., Lin, G., An, Z., 2022b. Effects of plant types on terrestrial leaf wax long-chain n-alkane biomarkers: Implications and paleoapplications. *Earth Sci. Rev.* 235, 104248.
- Mackay, D., Shiu, W.Y., Ma, K.C., Lee, S.C., 2006. *Handbook of Physical-Chemical Properties and Environmental Fate for Organic Chemicals* (2nd Ed.): Chapter 4 Polynuclear Aromatic Hydrocarbons (PAHs) and Related Aromatic Hydrocarbons. CRC Press, Boca Raton, p. 304.
- Mahowald, N., Jickells, T.D., Baker, A.R., Artaxo, P., Benitez-Nelson, C.R., Bergametti, G., Bond, T.C., Chen, Y., Cohen, D.D., Herut, B., Kubilay, N., Losno, R., Luo, C., Maenhaut, W., McGee, K.A., Okin, G.S., Siefert, R.L., Tsukuda, S., 2008. Global distribution of atmospheric phosphorus sources, concentrations and deposition rates, and anthropogenic impacts. *Global Biogeochem. Cycles* 22 (4), GB4026.
- Marlon, J.R., 2020. What the past can say about the present and future of fire. *Quatern. Res.* 96, 66–87.
- Marynowski, L., Simoneit, B.R.T., 2009. Widespread Upper Triassic to Lower Jurassic wildfire records from Poland: evidence from charcoal and pyrolytic polycyclic aromatic hydrocarbons. *Palaios* 24 (12), 785–798.
- Marynowski, L., Scott, A.C., Zatoń, M., Parent, H., Garrido, A.C., 2011. First multi-proxy record of Jurassic wildfires from Gondwana: evidence from the Middle Jurassic of the Neuquén Basin, Argentina. *Palaeogeogr. Palaeoclimatol. Palaeoecol.* 299 (1–2), 129–136.
- McLauchlan, K.K., Higuera, P.E., Miesel, J., Rogers, B.M., Schweitzer, J., Shuman, J.K., Tepley, A.J., Varner, J.M., Veblen, T.T., Adalsteinsson, S.A., Balch, J.K., Baker, P., Battlori, E., Bigio, E., Brando, P., Cattau, M., Chipman, M.L., Coen, J., Crandall, R., Daniels, L., Enright, N., Gross, W.S., Harvey, B.J., Hatten, J.A., Hermann, S., Hewitt, R.E., Kobzár, L.N., Landesmann, J.B., Loranty, M.M., Maezumi, S.Y., Mearns, L., Moritz, M., Myers, J.A., Pausas, J.G., Pellegrini, A.F.A., Platt, W.J., Roozeboom, J., Safford, H., Santos, F., Scheller, R.M., Sheriff, R.L., Smith, K.G., Smith, M.D., Watts, A.C., Durigan, G., 2020. Fire as a fundamental ecological process: Research advances and frontiers. *J. Ecol.* 108 (5), 2047–2069.
- Meyers, P.A., Ishiwatari, R., 1993. Lacustrine organic geochemistry—An overview of indicators of organic matter sources and diagenesis in lake sediments. *Org. Geochem.* 20 (7), 867–900.
- Mills, B.J.W., Krause, A.J., Jarvis, I., Cramer, B.D., 2023. Evolution of atmospheric O₂ through the Phanerozoic, revisited. *Annu. Rev. Earth Planet. Sci.* 51 (1), 253–276.
- Moroeng, O.M., Moore, T.A., Shen, J., Esterle, J.S., Liu, J., 2025. Isotopic and petrographic implications for fire type, temperature and formation of degradosemisulfite in fusain layers from an early cretaceous coal bed, Hailar Basin, Inner Mongolia, China. *Fuel* 384, 133895.
- Nádudvari, A., Misz-Kennan, M., Fabiańska, M., Ciesielczuk, J., Krzykowski, T., Simoneit, B.R.T., Marynowski, L., 2023. Preservation of labile organic compounds in sapropelic coals from the Upper Silesian Coal Basin, Poland. *Int. J. Coal Geol.* 267, 104186.
- Peel, M.C., Finlayson, B.L., McMahon, T.A., 2007. Updated world map of the Koppen-Geiger climate classification. *Hydrol. Earth Syst. Sci.* 11 (5), 1633–1644.
- Petersen, H.I., 1998. Morphology, formation and palaeo-environmental implications of naturally formed char particles in coals and carbonaceous mudstones. *Fuel* 77 (11), 1177–1183.
- Pickel, W., Kus, J., Flores, D., Kalaitzidis, S., Christianis, K., Cardott, B.J., Misz-Kennan, M., Rodrigues, S., Hentschel, A., Hamor-Vido, M., Crosdale, P., Wagner, N., 2017. Classification of lignite – ICCP System 1994. *Int. J. Coal Geol.* 169, 40–61.
- Sage, R.F., 2004. The evolution of C₄ photosynthesis. *New Phytol.* 161 (2), 341–370.
- Scotese, C.R., Wright, N., 2018. PALEOMAP Paleodigital Elevation Models(PaleoDEM) for the Phanerozoic PALEOMAP Project. <https://www.earthbyte.org/paleodem-resource-scotese-and-wright-2018/>.
- Scotese, C.R., Song, H., Mills, B.J.W., van der Meer, D.G., 2021. Phanerozoic paleotemperatures: the earth's changing climate during the last 540 million years. *Earth Sci. Rev.* 215, 103503.
- Scott, A.C., 1989. Observations on the nature and origin of fusain. *Int. J. Coal Geol.* 12 (Suppl), 443–475.
- Scott, A.C., 2000. The Pre-Quaternary history of fire. *Palaeogeogr. Palaeoclimatol. Palaeoecol.* 164 (1–4), 281–329.
- Scott, A.C., 2010. Charcoal recognition, taphonomy and uses in palaeoenvironmental analysis. *Palaeogeogr. Palaeoclimatol. Palaeoecol.* 291 (1–2), 11–39.
- Scott, A.C., Glasspool, I.J., 2007. Observations and experiments on the origin and formation of inertinite group macerals. *Int. J. Coal Geol.* 70 (1–3), 53–66.
- Shao, L., Zhou, J., Jones, T.P., Hua, F., Xu, X., Yan, Z., Hou, H., Wang, D., Lu, J., 2024. Inertinite in coal and its geoenvironmental significance: Insights from AI and big data analysis. *Sci. China Earth Sci.* 67 (06), 1779–1801.
- Stach, E.M., Mackowsky, T.M., Teichmüller, G.H., Taylor, D., Sfuftgarf, 1982. Stach's Textbook of Coal Petrology. Gebruder borntraeger, Berlin, p. 535.
- Street-Perrrott, F.A., Ficken, K.J., Huang, Y., Eglington, G., 2004. Late Quaternary changes in carbon cycling on Mt. Kenya, East Africa: an overview of the δ¹³C record in lacustrine organic matter. *Quat. Sci. Rev.* 23 (7), 861–879.
- Sýkorová, I., Pickel, W., Christianis, K., Wolf, M., Taylor, G.H., Flores, D., 2005. Classification of huminite—ICCP System 1994. *Int. J. Coal Geol.* 62 (1–2), 85–106.
- Taylor, G.H., Teichmüller, M., Davis, A., Diessel, C.F.K., Robert, P., 1998. Organic Petrology. Gebruder borntraeger, Berlin, p. 704.
- Vakhrameev, V.A., 1991. *Jurassic and Cretaceous Floras and Climates of the Earth*. Cambridge University Press, Cambridge, p. 340.
- Van Konijnenburg-Van Cittert, 2002. Ecology of some Late Triassic to Early Cretaceous ferns in Eurasia. *Rev. Palaeobot. Palynol.* 119 (1), 113–124.
- Wang, S.J., Tang, X.Y., Zhang, J., Yu, B., 1997. Jurassic coal-forming plants in Tuha basin and its relationship with oil from coal. *Coal Geol. Explor.* 06, 28–30 (in Chinese with English abstract).
- Wang, D., Yin, L., Shao, L., Lyu, D., Liu, H., Wang, S., Dong, G., 2021. Characteristics and evolution of inertinite abundance and atmospheric pO₂ during China's coal-forming periods. *J Palaeogeogr. English* 10 (2), 259–283.
- WMO, 2024. State of the Global Climate 2023: World Meteorological Organization. WMO-No. 1347.
- Wu, J., Ding, S., Li, Q., Sun, B., Wang, Y., 2016. Reconstructing paleoatmospheric CO₂ levels based on fossil Ginkgoites from the Upper Triassic and Middle Jurassic in Northwest China. *Paleontol. Z.* 90 (2), 377–387.
- Xie, W., Tan, J., Wang, W., Jia, J., Liu, Z., Wu, J., Wang, Y., Song, X., 2022. Record of Middle Jurassic wildfire and its incidental mercury emissions in northern Qaidam Basin, China: evidence from the inertinite and mercury anomalies in coal. *Int. J. Coal Geol.* 261, 104078.
- Xu, Y., Uhl, D., Zhang, N., Zhao, C.L., Qin, S.J., Liang, H.D., Sun, Y.Z., 2020. Evidence of widespread wildfires in coal seams from the Middle Jurassic of Northwest China and its impact on paleoclimate. *Palaeogeogr. Palaeoclimatol. Palaeoecol.* 559, 109819.
- Xu, X., Shao, L., Eriksson, K.A., Zhou, J., Wang, D., Hou, H., Hilton, J., Wang, S., Lu, J., Jones, T.P., 2022. Widespread wildfires linked to early Albian Ocean Anoxic Event 1b: evidence from the Fuxin lacustrine basin, NE China. *Global Planet. Change* 215, 103858.
- Yang, Y.K., 1996. *Atlas for Coal Petrography of China*. China University of Mining and Technology Press, Xuzhou, p. 321 (in Chinese).
- Yang, B., Zhang, X., Li, W., Sun, S., Yi, J., 2024. Palynological record of the Aalenian–Bajocian Cooling Event from the Santanghu Basin, Northwest China. *Diversity* 16, 369.
- Yunker, M.B., Macdonald, R.W., Vingazan, R., Mitchell, R.H., Goyette, D., Sylvestre, S., 2002. PAHs in the Fraser River basin: a critical appraisal of PAH ratios as indicators of PAH source and composition. *Org. Geochem.* 33 (4), 489–515.
- Yunker, M.B., Perreault, A., Lowe, C.J., 2012. Source apportionment of elevated PAH concentrations in sediments near deep marine outfalls in Esquimalt and Victoria, BC, Canada: is coal from an 1891 shipwreck the source? *Org. Geochem.* 46, 12–37.
- Zakir Hossain, H.M., Sampel, Y., Roser, B.P., 2013. Polycyclic aromatic hydrocarbons (PAHs) in late Eocene to early Pleistocene mudstones of the Sylhet succession, NE Bengal Basin, Bangladesh: Implications for source and paleoclimate conditions during Himalayan uplift. *Org. Geochem.* 56, 25–39.
- Zhang, Z., Wang, C., Lv, D., Hay, W.W., Wang, T., Cao, S., 2020. Precession-scale climate forcing of peatland wildfires during the early middle Jurassic greenhouse period. *Global Planet. Change* 184, 103051.
- Zhang, L., Yan, D., Yang, S., Li, B., Fu, H., Wang, G., Yang, X., Zhang, B., Liang, W., Zhang, J., 2023. Evolution of the Middle Jurassic paleoclimate: Sedimentary evidence from coal-bearing strata in the Santanghu Basin, NW China. *J. Asian Earth Sci.* 242, 105495.
- Zhao, Z., Guo, Z., Zhang, C., Lu, J., 2003. Tectonic evolution of the Santanghu Basin, East Xinjiang and its implication for the hydrocarbon accumulation. *Acta Sci. Nat. Univ. Pekin.* 39 (2), 219–228.
- Zhao, C., Zhang, K., Xiao, L., Uhl, D., Shi, Z., Zhao, W., Zhao, Q., Sun, Y., Liu, B., 2023. Paleoclimate-induced wildfires in a paleomire in the Ordos Basin, Northern China during the Middle Jurassic greenhouse period. *Chem. Geol.* 637, 121677.
- Zheng, B., Ciais, P., Chevallier, F., Yang, H., Canadell, J.G., Chen, Y., van der Velde, I.R., Aben, I., Chuvieco, E., Davis, S.J., Deeter, M., Hong, C., Kong, Y., Li, H., Li, H., Lin, X., He, K., Zhang, Q., 2023. Record-high CO₂ emissions from boreal fires in 2021. *Science* 379 (6635), 912–917.
- Zhong, X.C., Zhao, C.B., Yang, S.Z., Shen, H., 2003. *Jurassic System in the North of China. Volume II: Palaeoenvironment and Oil-Gas Source* (in Chinese). Petroleum Industry Press, Beijing, p. 214.
- Zhou, J., Shao, L., Jones, T.P., Huang, Y., Chen, M., Hou, H., Lu, J., Hilton, J., 2024. Mechanisms of inertinite enrichment in Jurassic coals: Insights from a big Data-driven review. *Earth Sci. Rev.* 257, 104889.